

# Low Mach number modeling of Type I X-ray burst deflagrations

David J. Lin

*Northwestern University, Department of Physics and Astronomy, 2145 Sheridan Road,  
Evanston, IL 60208, USA*

d-lin@northwestern.edu

Alvin Bayliss

*Northwestern University, Department of Engineering Sciences and Applied Mathematics,  
2145 Sheridan Road, Evanston, IL 60208, USA*

a-bayliss@northwestern.edu

and

Ronald E. Taam

*Northwestern University, Department of Physics and Astronomy, 2145 Sheridan Road,  
Evanston, IL 60208, USA*

r-taam@northwestern.edu

## Abstract

The Low Mach Number Approximation (LMNA) is applied to 2D hydrodynamical modeling of Type I X-ray bursts on a rectangular patch on the surface of a non-rotating neutron star. Because such phenomena involve decidedly subsonic flows, the timestep increase offered by the LMNA makes routine simulations of these deflagrations feasible in an environment where strong gravity produces significant stratification, while allowing for potentially significant lateral differences in temperature and density. The model is employed to simulate the heating, peak, and initial cooling stages in the deep envelope layers of a burst. During the deflagration, Bénard-like cells naturally fill up a vertically expanding convective layer. The Mach number is always less than 0.15 throughout the simulation, thus justifying the low Mach number approximation. While the convective layer is superadiabatic on average, significant fluctuations in adiabaticity occur within it on subconvective timescales. Due to convective layer expansion, significant compositional mixing naturally occurs, but tracer particle penetration through

the convective layer boundaries on convective timescales is temporary and spatially limited. Thus, mixing occurs on the relatively slow burst timescale through thermal expansion of the convective layer rather than from mass penetration of the convective layer boundary through particle convection. At the convective layer boundaries where mixing is less efficient, the actual temperature gradient more closely follows the Ledoux criteria.

*Subject headings:* convection — hydrodynamics — methods: numerical — stars: neutron — X-rays: bursts

## 1. Introduction

In the thermonuclear flash model, Type I X-ray bursts (henceforth referred to as *bursts*) are understood to be caused by the explosive ignition of hydrogen and/or helium gas, which have accreted onto the outer surface of neutron stars from relatively low-mass, binary companion donors. Extensive theoretical calculations using diffusional-thermal and 1D hydrodynamical models have successfully reproduced many of the general observational features of these bursts, such as the energies involved ( $\sim 10^{38}$ - $10^{39}$  ergs), their rise times (seconds), durations ( $\sim 10$ -100 seconds), spectral softening, and recurrence intervals (several hours). (For reviews, see Taam 1985, Lewin et al. 1995, Cumming 2004, and Strohmayer & Bildsten 2006.) However, multidimensional hydrodynamic modeling of bursts has been much more limited, partly due to limitations in computational resources. Using FLASH (Fryxell et al. 2000) based on the Piecewise Parabolic Method (PPM) (Colella & Woodward 1984), Zingale et al. (2001) simulated bursts as 2D detonations, albeit assuming very low mass accretion rates. Also using FLASH, Zingale et al. (2002) simulated bursts as 2D deflagrations using an artificial temperature perturbation in lieu of a realistic burning network. Spitkovsky et al. (2002) used the shallow water approximation to examine how flames would propagate during bursts around a two-layer neutron star surface, but their method is incompressible, assumes an ideal gas law, and does not account for thermal diffusion. In a different context, Dearborn et al. (2006) studied the related helium flash problem in the 3D cores of evolved giant stars using Djehuty (Bazán 2003), which is based on an explicit Lagrange-Eulerian hydrodynamic method.

Our current modeling effort simulates the heating, peak, and initial cooling stages of the deep envelope layers undergoing a burst with 2D hydrodynamics using the Low Mach Number Approximation (LMNA) and remedies the shortcomings of previous work in several respects: (1) compressibility effects are included; (2) potentially significant lateral fluctuations in temperature and density are allowed; (3) the essential input physics are considered,

including thermal diffusion, a realistic equation of state, and a burning network (a  $3\alpha$  nuclear burning network is reported here for simplicity, and more complete networks can be included); (4) no assumption is made regarding the nature of convection; (5) sound waves are naturally excluded from the domain, thereby eliminating both the acoustic timestep restriction and acoustic boundary reflection problems which can plague fully compressible simulations; and, (6) the computational time is reduced by a factor of 10-100 compared to fully compressible methods, due to the corresponding increase in the timestep.

Other approximation methods which eliminate the acoustic timestep restriction include the Boussinesq approximation (Spiegel & Veronis 1959; Miralles 2000), the anelastic approximation (Ogura & Phillips 1962; Glatzmaier 1984), and implicit methods (e.g., Deupree 2000). However, at present only the LMNA can successfully model the compressibility effects and significant lateral fluctuations in temperature and density which characterize deflagrations, as well as offer substantial increases in timestep and avoid acoustic boundary complications. While the LMNA is routinely used to model terrestrial combustion (e.g., Bayliss et al. 1992; McGrattan et al. 2004), only recently have efforts begun to adapt it to the astrophysical setting. Alternative astrophysical LMNA models have been recently developed by Bell et al. (2004a) and Almgren et al. (2006a, 2006b). Thus far, they have been used to examine 2D Landau-Darrieus planar flame instabilities during the early development of a Type Ia supernova (Bell et al. 2004b), Rayleigh-Taylor unstable flames in 2D and 3D (Bell et al. 2004c; Zingale 2005), and tested against the anelastic approximation and other fully compressible methods in a regime where all are valid (Almgren et al. 2006a, 2006b). The model by Bell et al. neglects background stratification, because the domain on which it was applied was much smaller than one pressure scale height. The model by Almgren et al. does include background stratification, and is thus more comparable to ours. However, our LMNA model differs from Almgren et al.’s in several important respects: (1) they evolve the density via the continuity equation, whereas we evolve the temperature via the energy equation; (2) they neglect thermal diffusion, because it is expected to be unimportant in their modeling of Type Ia supernova, whereas we include it in our model; (3) they allow a time-dependent background state, while presently, we assume it is time-independent, a condition which is easily relaxed and is reserved for future work; (4) we reformulate (using a novel function which will be described in detail below) the perturbative pressure gradient and buoyancy forces to accurately calculate the net vertical force in the presence of significant cancellation for large gravity.

In §2, the motivation and essence of our LMNA model are presented. The results of applying the LMNA to simulate a Type I X-ray burst in 2D are described in §3. Next, §4 briefly describes verification studies which were performed. Finally, a discussion of the key findings and limitations of the present model, along with ideas for future development and

applications, is presented in §5.

## 2. Computational procedure

Weakly compressible (low Mach number) models have been extensively employed in studies of terrestrial combustion. Such models are suitable for low speed deflagrations. They account for thermal expansion of the gas, but assume only weak compressibility. As such they allow a filtering of sound waves from the hydrodynamic equations so that timesteps employed in computational methods can be based on the local fluid velocity rather than the (much larger) sound speed.

The essence of such models is to expand the hydrodynamic quantities around a mean state with perturbations proportional to  $M^2$ , where  $M$  is the maximum local Mach number:

$$A \simeq A^0 + M^2 A'.$$

Here,  $A$  is the non-dimensionalized form of any of the hydrodynamic quantities (density  $\rho$ , velocity  $\mathbf{v}$ , pressure  $P$ , temperature  $T$ , and mass fractions  $X_l$  of species  $l$  in the gas). This expansion is then incorporated into the hydrodynamical equations (either reacting Euler or reacting Navier-Stokes equations, together with the equation of state). In terrestrial combustion, the zeroth order pressure  $P^0$  can be shown to be independent of the spatial coordinates, and for an open system,  $P^0$  is independent of time as well. Under the low Mach number assumption, the pressure perturbation  $P'$  appears only in the momentum equation, and the pressure  $P$  is assumed to be equal to the constant  $P^0$  in the energy and state equations. All other variables are solved only for the zeroth order quantities. Thus, the primary approximation in the low Mach number model is the use of the base pressure in the equations of state and energy. Since the equation of state involves a relationship between  $\rho$  and  $T$ , generally both the energy equation and the continuity equation are not solved in the computational model. Rather one of these equations is solved and the other employed as a constraint together with the momentum equation to develop an elliptic equation for the pressure perturbation  $P'$ . Different choices have been described in the literature (see below).

In the neutron star configurations considered here, the deflagrations do not occur under isobaric conditions due to large vertical pressure stratifications, so a more appropriate base state is one of hydrostatic equilibrium. In our model, all hydrodynamic quantities are expanded around a precomputed hydrostatic base state, which is assumed to be independent of time, although that assumption can be readily relaxed. That is, for any of the hydrodynamic quantities,

$$A(\mathbf{r}, t) = A_h(z) + A'(\mathbf{r}, t), \quad (1)$$

where  $\mathbf{r}$  is the position vector,  $t$  is time,  $z$  is the vertical direction, and  $A_h(z)$  represents the hydrostatic base state of the hydrodynamic quantity. Only the hydrostatic pressure  $P_h(z)$  is kept in the equation of state and the energy equation, thereby filtering out sound waves. The equations of the model are solved directly for the physical variables since due to the wide range of scales involved (e.g.,  $22 < \log P < 24$ ; ref. Fig. 1), non-dimensionalization is not particularly useful. In the expansion (eq. [1]) the only perturbed quantity is  $P'$ . The fundamental assumption in the model is that  $P'$  is small compared to  $P_h$  and can be neglected in the equations of state and energy. No assumptions are made regarding the magnitude of  $\rho'$  and  $T'$ . They are defined as  $\rho' = \rho - \rho_h$  and  $T' = T - T_h$  respectively so that effectively we solve for the full density and temperature in our model. The introduction of the primed variables is simply a computational device to explicitly incorporate the hydrostatic equilibrium base state and eliminate numerical errors due to the cancellation of large quantities in the vertical momentum equation. As an ex-post-facto justification of the assumption, we verified that  $M < 0.15$  throughout the simulation and that  $|P'/P_h| \leq M^2$ , often decidedly less.

In principle, a laterally varying base state can be incorporated in the model. However, in this case a lateral flow field would be set up due to the lateral pressure gradients. Such a flow field would then result in a vertical flow field so that the resulting base state would no longer be in hydrostatic equilibrium. In view of the large values of  $g$ , any significant imbalance between the pressure gradient and buoyancy term in the vertical momentum equation would necessarily result in large velocities inconsistent with the assumptions of the low Mach number model. Hence,  $P_h$  is laterally independent in our LMNA model.

We next describe the equations of the model. By substituting equation (1) into the Euler equations, the LMNA governing equations are obtained and presented in the order in which they are solved:

$$\frac{DX_l}{Dt} = R_l, \quad (2)$$

$$\rho c_p \frac{DT}{Dt} - \delta \frac{DP_h}{Dt} = Q + \nabla \cdot \kappa \nabla T - \sum_l \rho \frac{\partial H}{\partial X_l} R_l, \quad (3)$$

$$\rho = F(T, P_h, X_l), \quad (4)$$

$$\rho \frac{D\mathbf{v}}{Dt} + \nabla P' = \rho' \mathbf{g}. \quad (5)$$

These expressions are the equations of species (eq. [2]), energy (eq. [3]), state (eq. [4]), and momentum (eq. [5]). Here,  $\frac{D}{Dt}$  is the material derivative;  $\mathbf{g}$  is the gravitational acceleration vector ( $= -g\hat{\mathbf{k}}$  in the vertical direction), where  $g$  is assumed to be a constant, since its value changes by only 0.1% over the vertical extent presently modeled;  $c_p$  is the specific heat at constant pressure;  $\delta$  is a thermodynamic coefficient  $= -\left(\frac{\partial \ln \rho}{\partial \ln T}\right)_P$ ;  $Q$  is the  $3\alpha$  rate of energy generation per unit volume;  $H$  is the enthalpy;  $R_l$  is the rate of production and depletion of species  $l$ ; and  $\kappa$  is the radiative thermal conductivity  $= \frac{4}{3} \frac{acT^3}{\kappa_o \rho}$ , where  $a$  is the radiation constant,  $c$  is the speed of light, and  $\kappa_o$  is the radiative opacity, calculated from analytical expressions as referenced in Iben (1975), Christy (1966), and Weaver et al. (1978). The tabulated Helmholtz equation of state (Timmes & Swesty 2000) of an ionized gas includes the contributions of radiation as well as electrons in an arbitrary state of degeneracy. The energy generation rate (EGR) is obtained from the S-matrix calculations of Fushiki & Lamb (1987) which includes electron screening factors. Subsequent  $\alpha$ -capture reactions involving  $^{12}_6\text{C}$  are neglected, since calculations show that the EGR of these reactions before the peak of the burst are negligible compared to that of the  $3\alpha$  reaction. Base state hydrostatic equilibrium ( $\nabla P_h = -\rho_h \mathbf{g}$ ) is employed in equation (3). Fluid viscosity is neglected in view of the large Reynolds numbers expected on the neutron star.

On the right-hand-side of the energy equation (eq. [3]),  $\sum_l \rho \frac{\partial H}{\partial X_l} R_l$  is the change in energy due to the change in composition. We have investigated this term and found that its effect is negligible. We therefore do not include it in our computations due to the extra computational cost required for its evaluation in the equation of state.

Note that  $P'$  appears only in the momentum equation (eq. [5]). Generally, cancellation between the perturbed pressure gradient and the  $\rho' \mathbf{g}$  buoyancy term occurs, which can result in significant numerical errors, compounded by the large values of  $g$ . The accuracy and stability of the computation is significantly enhanced by introducing the variable

$$\phi = P' - gK, \quad K = \int_{z_{top}}^z \rho' dz' \quad (6)$$

where  $K$  is an integrated density function, which is calculated per lateral column from the top of the domain ( $z_{top}$ ) downward. Using  $\phi$ , the momentum equation (eq. [5]) can be equivalently expressed as

$$\rho \frac{D\mathbf{v}}{Dt} = -\nabla \phi - \frac{\partial(gK)}{\partial y} \hat{\mathbf{j}}. \quad (7)$$

Note that  $\nabla\phi$  represents the net vertical force per unit volume so that in this formulation, cancellation between the perturbed pressure gradient and the  $\rho'\mathbf{g}$  buoyancy term is explicitly accounted for. A term proportional to  $g$  now enters into the lateral momentum equation, which we have found does not cause numerical difficulties.

By taking the divergence of the momentum equation (eq. [5]) and using the continuity equation ( $\frac{\partial\rho}{\partial t} + \nabla \cdot \rho\mathbf{v} = 0$ ), an elliptic equation is obtained:

$$\nabla^2\phi = \frac{\partial^2\rho}{\partial t^2} - \nabla \cdot \{\nabla \cdot (\rho\mathbf{v}\mathbf{v})\} - \frac{\partial^2(gK)}{\partial y^2}. \quad (8)$$

Solving the elliptic equation is necessary to close the set of governing equations. Note that temperature is explicitly evolved with the energy equation (eq. [3]) but the continuity equation is not solved directly. Density and temperature are related via the equation of state for constant  $P_h$ . Since we enforce the equation of state, density and temperature cannot be updated independently of one another. As a result, either the continuity or energy equation can be included in the equations of the model; the other equation is incorporated in the compressibility constraint, that is, the use of the continuity equation in the energy equation for terms involving the divergence of the velocity field, ultimately leading to the right-hand side of equation (8). The equation of state is used to relate density, temperature and mass fraction. (An alternative formulation, relaxing the equation of state is described in Bell et al. 2004a.) In terrestrial modeling, different approaches have been adopted in the literature. Some approaches (e.g., McMurtry et. al. 1985; McGrattan et. al. 1994, 2000, 2004, and the references therein) solve the continuity equation and eliminate the energy equation, incorporating it into the compressibility constraint. Other approaches (e.g., Majda and Sethian 1985; Bayliss et al. 1992) solve the energy equation, employing the continuity equation as a constraint. We adopt the latter approach. The alternative formulation causes numerical difficulties in obtaining the density from the equation of state due to the weak temperature dependence of the pressure for the degenerate conditions that pertain during the burst.

Using the continuity equation, the term  $\frac{\partial^2\rho}{\partial t^2}$  in equation (8) is numerically evaluated as:

$$\frac{\partial^2\rho}{\partial t^2} = \frac{1}{\Delta t} \left[ \left( \frac{\partial\rho}{\partial t} \right)^{n+1} + \nabla \cdot (\rho\mathbf{v})^n \right], \quad (9)$$

where  $\Delta t$  is the time step,  $n$  denotes values at the current time-level, and  $n + 1$  denotes values at the next time-level. Here,  $\left( \frac{\partial\rho}{\partial t} \right)^{n+1}$  is determined from an analytical expression for  $\frac{\partial\rho}{\partial t}$  which can be obtained from evaluating the partial derivatives of the internal energy. On the other hand,  $\nabla \cdot (\rho\mathbf{v})^n$  is evaluated by centrally differencing local values of  $\rho$  and  $\mathbf{v}$  at

the present time-level over two zones. Solving equation (9) in this manner is required for numerical stability.

The governing equations are solved with operator-splitting on a uniform, staggered, plane-parallel, Cartesian grid which is parallelized using the Message-Passing Interface (MPI) software. Upwind (advective and first-order convective terms (terms having the form  $\mathbf{v} \cdot \nabla \mathbf{v}$ , see the Appendix below)) and central differencing (diffusion,  $gK$ , and second-order convective terms) are used for spatial derivatives. When needed, linear averaging is used, for instance, to find zone center values from zone edge values. Forward-Euler is used to difference time derivatives, using a Courant factor (the proportionality constant which is required for numerical stability and relates the local timestep, zone size, and propagation speed) of 0.50, which is comparable to Courant factors employed in fully compressible 2D calculations. Thus, the current model is first-order accurate in space and time, however, a second order in time scheme can be easily implemented as a predictor-corrector scheme (e.g., McGrattan et al 2004). In such a scheme a predicted value is first computed at the new timestep. In the corrector step, central differences in time are assumed analogous to the midpoint method, thereby resulting in second order temporal accuracy. We have tested such a predictor-corrector scheme and found that there was only a negligible effect on the solution. Since the predictor-corrector scheme essentially doubles the cost of the computation, we do not use it in our computational scheme. This elliptic equation for  $\phi$  (eq. [8]) is solved using FISHPAK, a package of subprograms for the solution of separable, elliptic partial differential equations developed by Adams, Swarztrauber, and Sweet (1988).

The timestep is determined adaptively from the solution. At each step, the smallest timestep based on the flow speed ( $dt_{CFL}$ ), thermal diffusion, and nuclear burning in the entire domain is compared to a fixed, maximum timestep  $dt_{max}$  (a parameter, chosen to be  $5 \times 10^{-6}$  s), and the smallest one becomes the timestep for the next computational step. Numerical stability requires using  $dt_{max}$ , and its necessity is related to the large value of  $g$  in this problem. Only during the initial part of the simulation does  $dt_{max}$  dominate over the other timesteps, and for the remainder of the simulation,  $dt_{CFL}$  dominates. Also, the maximum allowed percentage increase in timestep is 10% above the previous value.

For the initial conditions,  $10^3$  cm of a neutron star envelope is constructed in thermal and hydrostatic equilibrium in the manner of Bildsten (1995) with a 1 cm/zone resolution. Canonical neutron star parameters are chosen:  $M_{NS} = 1.4M_{\odot}$ ,  $R_{NS} = 1.0 \times 10^6$  cm, and  $g = \frac{GM_{NS}}{R_{NS}^2} = 2 \times 10^{14}$  cm s $^{-2}$ . (We note that  $g$  is large, thereby warranting special numerical procedures as described above to deal with cancellation between the pressure gradient and buoyancy force in the vertical momentum equation of the 2D model.) The mass accretion rate per unit area is  $\dot{m} = \frac{5 \times 10^{-9}}{4\pi R_{NS}^2} M_{\odot} \text{ yr}^{-1} \text{ cm}^{-2}$ . We note that at such accretion rates, our



assumption of helium burning corresponds to the accretion of helium, rather than a hydrogen rich composition. Such a circumstance could apply to the case of ultra compact low mass X-ray binary systems (see, for example, Nelemans & Jonker 2006). The flux at the base of the model is chosen to be  $5 \times 10^{20} \text{ erg s}^{-1} \text{ cm}^{-2}$ , a value corresponding to crustal heating associated with residual nuclear burning. (Changing this value affects the depth at which the burst occurs.) This initial structure is used in the 2D model as the reference base state ( $P_h, T_h, \rho_h$ ). To generate the starting conditions for the 2D hydrodynamical evolution, the initial structure is first evolved with a 1D diffusional-thermal code (which solves eqs. [2], [3], and [4]) through several burst cycles with hydrostatic equilibrium re-calculated after each timestep. From this, subadiabatic conditions which exist approximately 1 s prior to the peak of the burst become the starting conditions for the 2D model. This 1D structure is reproduced across the width of the computational domain to create a laterally uniform 2D domain. While several domain dimensions were tested, the domain used for the results presented here has  $386 \times 200$  zones at a resolution of 5 cm/zone. To save on computational expense, the upper boundary of the 2D domain is 500 cm below the actual surface of the star, which is not modeled.

Initially, as shown in Figure 1, the domain extends over one order of magnitude in  $\rho$  ( $10^6$ -  $10^7 \text{ g cm}^{-3}$ ) and nearly two orders of magnitude in  $P$  ( $10^{22}$ -  $10^{24} \text{ erg cm}^{-3}$ ) corresponding to 4.5 pressure scale heights ( $H_P \sim 200 \text{ cm}$ ). Since thermal and compositional histories are taken into account from the diffusional-thermal evolution, Figure 2 shows that the temperature profile has a local maximum and inversion where the burst ignites from the hottest layer. The initial maximum value of  $T$  is  $2 \times 10^8 \text{ K}$ , which corresponds to an initial maximum EGR of  $7 \times 10^{14} \text{ erg g}^{-1} \text{ s}^{-1}$ . Figure 2 also shows a very steep gradient in  $Y$  ( ${}^4_2\text{He}$  mass fraction) occurring where the hottest layer is located, such that  $Y \sim 0.98$  above and  $Y \sim 0.02$  below. Because only two species are considered, the ash complement is  $Z$  ( ${}^{12}_6\text{C}$  mass fraction).

It is important to note that the hottest burning layer corresponds to a density of  $\sim 4 \times 10^6 \text{ g cm}^{-3}$ , and that the density at the top of the computational domain is of order  $10^6 \text{ g cm}^{-3}$ . Thus, we do not model the lower density regions of the neutron star’s upper atmosphere, a region which extends 500 cm above the top of our computational domain. This region is not modeled for several reasons: 1) it requires a significantly smaller timestep, due to the timestep restriction associated with thermal diffusion, which reduces the time-savings advantage afforded by the LMNA approximation; 2) its lower densities facilitate the development of larger magnitude flows and hence larger Mach numbers, thus limiting the applicability of the LMNA model there; 3) its degeneracy is lifted at advanced stages of the burst, resulting in significant vertical expansion (e.g. Cumming and Bildsten 2000), thus requiring a time-dependent pressure base state to properly model, a feature which is

not incorporated into the current LMNA model, but which can be readily developed into future models. Because the current model examines relatively high density regions at depth, no significant expansion occurs in the model throughout most of the burst event, and a time-independent base state is sufficient.

To provide lateral inhomogeneity, a small, 2D Gaussian perturbation in density is applied ( $\left(\frac{\Delta\rho}{\rho}\right)_{max} = -1 \times 10^{-6}$ , full-width-half-max = 50 cm), such that the center of the perturbation is laterally centered and vertically positioned at the latitude of the hottest layer. Without this perturbation, the burst proceeds in a laterally homogeneous manner, and no 2D convective structures form. Thus, the purpose of the initial perturbation is merely to break the lateral symmetry of the starting conditions, allowing 2D dynamical structures to naturally develop during the subsequent evolution. As long as the magnitude of the perturbation in  $\rho$  is less than a fractional difference of  $10^{-2}$ , the subsequent dynamics is qualitatively independent of the magnitude and placement of the initial perturbation in the domain.

Periodicity is assumed at the lateral domain edges for all evolved variables. As verified by extensive numerical experiments, the domain's lateral size is sufficiently wide so as not to affect the size and evolution of the convection cells which naturally develop. At the lower boundary,  $\frac{\partial T}{\partial z}$ ,  $\frac{\partial \rho}{\partial z}$ ,  $\frac{\partial X_i}{\partial z}$ , and  $\frac{\partial v}{\partial z}$  are all set to zero, where  $v$  is the lateral component of the velocity. The vertical component of velocity  $w$  and all convective terms are set to zero. In the elliptic solver, the Neumann condition ( $\frac{\partial \phi}{\partial z} = 0$ ) is used, which is equivalent to imposing hydrostatic equilibrium at the lower boundary. The domain's lower edge is set sufficiently deep such that flows which develop there are relatively small ( $|\mathbf{v}| < 10^2 \text{ cm s}^{-1}$ ) compared to those in the convective layer ( $10^4 < |\mathbf{v}| < 10^7 \text{ cm s}^{-1}$ ). At the upper boundary,  $\frac{\partial v}{\partial z}$ ,  $\frac{\partial w}{\partial z}$ , and  $\frac{\partial X_i}{\partial z}$  are set to zero, and all convective terms are set to zero. A temperature flux condition  $\frac{\partial T}{\partial z} = -\frac{\rho T}{4N_{top}}$  is used to update  $T$ , where  $N_{top}$  is the column density at the upper boundary ( $N_{top} = \frac{P_{top}}{g}$ ). The temperature flux condition is derived from equating the radiative flux  $F = -\frac{4ac}{3\kappa\rho}T^3\frac{dT}{dz}$  with the surface flux  $F = \sigma T_{eff}^4$ , where  $T^4 = \frac{3}{4}T_{eff}^4(\tau + \frac{2}{3})$  and  $\tau = \int \kappa\rho dz = \frac{\kappa P}{g}$ . Here,  $T_{eff}$  is the effective temperature at the neutron star's surface. Also,  $F$  and  $\kappa$  are assumed to be constant in the region between the upper domain boundary and the actual surface of the star and that this region is in radiative equilibrium. A consistent  $\rho$  is then found via the equation of state. In the elliptic solver, the Dirichlet condition ( $\phi = 0$ ) is imposed. Since  $K = 0$  at the upper boundary (see eq. [6]), the Dirichlet condition is effectively a condition that  $P' = 0$  at the top. We note that the results are insensitive to the placement of the lower boundary, provided that it is sufficiently deep. Likewise, the results are insensitive to the location of the upper boundary, provided it is sufficiently high, except for a very weak sensitivity near burst peak. The boundary conditions described above allow for the burst and do not result in any noticeable numerical oscillations or numerical

instabilities.

A more detailed description of the computational model is given in the Appendix, as well as in Lin (2006).

### 3. Type I X-ray burst deflagrations

#### 3.1. Convective dynamics

The important thermodynamic and hydrodynamic features which develop during the burst calculation are first described. By way of definition, the subscript *max* indicates the instantaneous spatial maximum value of a quantity; the subscript *peak* indicates the greatest value of the quantity throughout the entire burst sequence; and the subscript *ave* indicates the spatially-averaged value of the quantity over a particular analysis period.

The value of  $\text{EGR}_{\text{max}}$  quantifies the burst evolution sequence, as shown in Figure 3, where  $\text{EGR}_{\text{max}}$  (solid line) is plotted as a function of time. The time  $t$  is given in terms of the physical time after the start of the calculation ( $t = 0$  s). Throughout the burst sequence,  $\text{EGR}_{\text{max}}$  can be found in a layer, henceforth referred to as the *burning layer*, the height of which is roughly constant throughout the burst progression at approximately 500 cm above the domain base and which corresponds to the height of the initially hottest layer of the starting conditions. At the peak of the burst,  $t = 1.572$  s and the peak value of the EGR during the entire sequence is  $\text{EGR}_{\text{peak}} = 2 \times 10^{19} \text{ erg g}^{-1} \text{ s}^{-1}$ . Simultaneously, the maximum flow speed also peaks at  $5 \times 10^7 \text{ cm s}^{-1}$  ( $M_{\text{peak}} = 0.15$ ; Fig.3 dashed line), which justifies using the LMNA to model this phenomenon. Fig. 4 shows the laterally averaged temperature as a function of height. As will be quantified below, the temperature gradient is nearly adiabatic in the vertically expanding layer where convection develops, and after the burst peak, adiabaticity is lost since the temperature profile eventually becomes more uniform in the upper domain resulting from the upward transport of heat by thermal diffusion. Due to heating terms still dominating cooling terms at the time of burst peak, the temperature peaks  $\sim 0.10$  s after the EGR peaks ( $T_{\text{peak}} = 1.7 \times 10^9 \text{ K}$ ).

Initially, everything is quiescent, since  $\nabla < \nabla_{\text{ad}}$  everywhere, where  $\nabla \equiv \left(\frac{d \ln T}{d \ln P}\right)_{\text{actual}}$  and  $\nabla_{\text{ad}} \equiv \left(\frac{d \ln T}{d \ln P}\right)_s$ , which is the adiabatic temperature gradient (Schwarzschild 1906). Lateral inhomogeneities introduced by the initial perturbation cause small-scale, localized eddies to develop everywhere in the domain. The magnitude of  $\mathbf{v}_{\text{ave}}$  of these eddies is on the order of  $10^2 \text{ cm s}^{-1}$ . At  $t = 0.15$  s ( $\log \text{EGR}_{\text{max}} = 14.9$ ), a thin layer approximately 50 cm in vertical extent becomes superadiabatic, such that  $(\Delta \nabla)_{\text{max}} = 0.12$  (where  $\Delta \nabla \equiv \nabla - \nabla_{\text{ad}}$ , the adiabatic excess), and by  $t = 0.35$  s ( $\log \text{EGR}_{\text{max}} = 15$ ), convective motions naturally develop

and become evident in this layer. At this time, the magnitude of  $\mathbf{v}_{ave}$  in the convective region is of order  $10^4 \text{ cm s}^{-1}$ , however the flow field initially lacks apparent structure. As the burst proceeds and  $\text{EGR}_{max}$  rises, the boundaries of the convective layer expand vertically due to thermal diffusion of heat away from the burning layer. By  $t = 0.70 \text{ s}$  ( $\log \text{EGR}_{max} = 15.2$ ), the vertical extent of the convective layer has increased to  $\sim 150 \text{ cm}$ , and the flow field self-organizes into distinct Bénard cells (Bénard 1900; Koschmieder 1993), each characterized by central upflows and adjacent downflows. The shapes and sizes of the convective cells are dynamically evolving on subconvective timescales, which varies from  $1000 \mu\text{s}$  (at  $\log \text{EGR}_{max} = 16$ ) to  $150 \mu\text{s}$  (at  $\log \text{EGR}_{max} = 19$ ).

Figure 5 shows flow fields superimposed against contours of superadiabaticity ( $\Delta\nabla$ ) in the domain at four stages prior to burst peak. For each plot in the figure, the vertical axis represents the vertical direction  $z$  (cm), and the horizontal axis measures the lateral direction  $y$  (cm). (The origin of the coordinate system is located at the lower left corner of the computational domain. The entire lateral width of the domain is shown in the figure, while the relatively calm, lower half of the domain is omitted for clarity.) To enhance the clarity of the main features in the flow fields, the resolution of the vector field is  $30 \text{ cm/zone}$ , that is, every 6th velocity vector is plotted.

At  $\log \text{EGR}_{max} = 16$  and  $17$  (Figs. 5a and 5b), distinct Bénard-like cells have self-organized, and the larger cells are approximately symmetric with uniform aspect ratios. The larger cells are characterized by central updrafts, which channel material from the base of the convective layer through vertical chimneys upward toward the top of the convective layer boundary. There, the flows laterally bifurcate to form more diffuse downdrafts. The flow fields dynamically evolve on a subconvective timescale. For example, a given larger cell may break up into smaller cells. Smaller cells may merge to form a larger cell. The direction of updrafts and downdrafts may also skew diagonally. The aspect ratio of a cell may momentarily change significantly, as the cell takes on a variety of shapes and forms, but maintaining its overall outline as a complete cell. An updraft occurring at one time at a certain lateral location may develop into a downdraft at the same location within a few convective times. No bulk lateral motion of the cells is apparent, as the individual cells do not hold their integrity long enough to noticeably drift as a unit. By the later stages of the burst ( $\log \text{EGR}_{max} = 18$  and  $18.5$ ; Fig. 5c and 5d), the convective layer noticeably expands due to thermal diffusion of heat away from the burning layer. The boundary of the upper convective layer propagates upward on the order of  $10^4 \text{ cm s}^{-1}$ , while the lower boundary moves downward at  $10^2 \text{ cm s}^{-1}$ . As the layer expands, the heights of the larger cells grow to fill up the vertical extent of the layer. Correspondingly, the horizontal widths of the larger cells also increase to maintain a roughly uniform aspect ratio. The cells continue to dynamically morph into a variety of shapes, orientations, and sizes on subconvective

timescales.

Standing out in bold contrast against the radiative regions above and below it, the convective layer can be seen in Figures 5 *a – d* to be superadiabatic on average, but with subadiabatic pockets within it. These subadiabatic regions can always be found in the convective layer throughout the evolution and become more distinct at higher  $\text{EGR}_{\text{max}}$  levels. The most superadiabatic regions appear to form near the bottom of the convective layer as elongated fronts which are carried up by the strongest currents to the top of the convective region. Laterally averaged over time, however, the convective layer is slightly superadiabatic (+0.01 pre-burst peak, +0.001 post-burst peak).

Figure 6 illustrates the laterally and temporally averaged, root-mean-square (RMS) values of  $v$  and  $w$  as functions of height at  $\log \text{EGR}_{\text{max}} = 18.5$ . For reference, the adiabatic excess is also plotted. At this particular stage in the burst evolution within the convective layer ( $\Delta \nabla > 0$ ),  $w_{\text{RMS}}$  peaks near the center of the layer, and diminishes by an order of magnitude at the layer boundaries. On the other hand, a local minimum in  $v_{\text{RMS}}$  occurs near the center of the layer, while  $v_{\text{RMS}}$  peaks toward the layer boundaries. This is consistent with the general nature of the flow in a Bénard-like cell. Notably, Figure 6 shows that on average,  $v_{\text{RMS}}$  exceeds  $w_{\text{RMS}}$  at the boundaries by nearly an order of magnitude. At other stages of the burst, the qualitative behavior of these quantities as a function of height is identical, but the range in magnitude may be as great as two orders of magnitude (e.g., when  $\log \text{EGR}_{\text{max}} < 17$ ). The dominance of lateral over vertical flows at the layer boundaries helps to explain the limited amount of tracer particle penetration beyond the convective layer boundaries (see below).

Figure 7 focuses on a Bénard-like cell at  $\log \text{EGR}_{\text{max}} = 17$ . Here, the flow field is superimposed against contours of temperature fluctuation, expressed with the notation

$$\Delta T \equiv T - T_{\text{ave}}(z),$$

where  $T$  is the instantaneous temperature at a given zone, and  $T_{\text{ave}}(z)$  is the lateral average at height  $z$ . (The fluctuation in  ${}^4\text{He}$  mass fraction  $\Delta Y$  is similarly defined.) Black velocity vectors are used where  $w > 0$ , while white vectors indicate where  $w < 0$ . The cell in Figure 7 exemplifies how upflows are generally associated with columns which are relatively warmer than their surroundings. Conversely, downflows are generally associated with slightly cooler regions. Regions which are relatively warmer are necessarily lower in density, and therefore rise due to buoyancy, resulting in upward flows, and vice versa. Upflows are generally more collimated than downflows. The flow fields and fluctuations vary on the same subconvective timescales. Moreover,  $\Delta T$  and  $\Delta Y$  are complementary at all times, such that up- and downflows are consistently characterized by deficits and excesses in  $Y$  respectively. As the

flow speeds increase, so do the magnitude of the fluctuations, and the maximum relative magnitude of these fluctuations throughout the entire burst is  $\pm 0.10$ .

The correlation between the sign of  $\Delta Y$  and the flow direction can be understood to be entirely an advective effect, since the timescales over which these fluctuations occur ( $\sim 10^{-5}$  -  $10^{-3}$  s) are many orders of magnitude smaller than burning timescales ( $\sim 10^{-1}$  s). To help explain this association, Figure 8 illustrates the profile of the percentage difference (PD =  $\Delta Y/Y_C$ , where  $\Delta Y = Y - Y_C$ ) of the laterally averaged value of  $Y$  with respect to  $Y_C$ , the value at the center of the convective region ( $z = 625$  cm) at  $\log \text{EGR}_{max} = 17$ . As the figure shows, convective mixing very efficiently homogenizes the composition in most of the convective layer, where  $Y$  varies by less than one percent over a height corresponding to one pressure scale height at this particular stage in the burst, and up to two pressure scale heights at more advanced stages. However, at the layer’s upper and lower boundaries, substantial composition gradients exist due to less efficient mixing there ( $\sim -5\%$  at the lower boundary,  $+5\%$  at the upper boundary). Lateral flows also dominate in these regions, as previously described. Thus, converging lateral flows at the sources of downflows locally concentrate fuel within a relatively rich helium layer near the convective layer’s upper boundary, and the vertical flows advect fuel downward. In the same manner at the lower boundary, local concentration of carbon ( $Y$  deficit) occurs at the source of upflows, where carbon is advected upward.

To help quantify the extent and evolution of the convective layer, the vertical velocity correlation function  $W$  is calculated in the manner of Chan & Sofia (1987):

$$W = \frac{\langle w_k w_{ref} \rangle}{\langle w_k \rangle^{1/2} \langle w_{ref} \rangle^{1/2}}.$$

The vertical velocity correlation  $W$  is constructed by laterally and temporally averaging the product of  $w$  at two vertical positions, one of which is a fixed reference position ( $w_{ref}$ ). For each EGR level, this reference position is taken to be at the same vertical height, corresponding to the center of the convective layer at  $\log \text{EGR}_{max} = 16$ .  $W$  has a bell-shaped structure, and it can be used to quantitatively define the positions of the vertical edges of the larger Bénard cells. With reference to both the Schwarzschild criteria ( $\nabla > \nabla_{ad}$ ) and the actual sizes of the larger cells which develop, the convective layer can be characterized by regions where  $W > 0.10$ . For example, Figure 9 shows the vertical expansion of the convective layer as represented by  $W$  plotted as a function of  $\ln P$  at four EGR levels leading up to the peak of the burst. By  $t = 1.5$  s ( $\log \text{EGR}_{max} = 17$ ), the vertical extent of the convective region is roughly one pressure scale height, and by burst peak at  $t = 1.572$  s ( $\log \text{EGR}_{max} = 19.2$ ), it has expanded to about two pressure scale heights. Also, the lateral velocity correlation function  $V$  is calculated using a reference position at the lateral center

of the domain. Comparing  $V$  with  $W$  shows that the ratio of lateral to vertical extents of the larger cells throughout the burst evolution varies between 0.9 and 1.1, such that on average, they feature a roughly uniform aspect ratio.

Figure 10 shows  $W$ ,  $\nabla$ ,  $\nabla_{ad}$ , and the Ledoux gradient  $\nabla_L \equiv \nabla_{ad} + \frac{c_1}{c_2} \nabla_\mu$  as a function of  $\ln P$  at  $\log \text{EGR}_{max} = 18$ , where  $\nabla_\mu \equiv \left(\frac{d \ln \mu}{d \ln P}\right)$ ,  $c_1 \equiv \left(\frac{\partial \ln \rho}{\partial \ln \mu}\right)_{P,T}$ ,  $c_2 \equiv -\left(\frac{\partial \ln \rho}{\partial \ln T}\right)_{P,\mu}$ , and  $\mu$  is the mean molecular weight. Here, as is true at all EGR levels, the convective layer is superadiabatic on average. Moreover, the actual temperature gradient more closely follows the Ledoux gradient near the convective layer boundaries, due to steep composition gradients which persist because convective mixing is less efficient there. The figure also shows a region near the base of the convective layer which satisfies the semiconvective criteria,  $\nabla > \nabla_L$  (Ledoux 1947). This region consistently satisfies the semiconvective criteria when  $\log \text{EGR}_{max} > 18$ .

Post-burst peak, the superadiabaticity of the convective layer decreases as more of the domain heats up and the temperature gradient moderates. Consequently, convective motions gradually diminish, and the Mach number falls. By the conclusion of the calculation ( $t = 1.74$  s), the domain has become completely subadiabatic again, and all convective motions cease. Residual motion occurs at the upper boundary, but these velocities are relatively insignificant ( $M_{max} < 0.02$ ).

### 3.2. Convective material transport

As the burst evolves, mixing of composition from radiative regions into the convective layer naturally occurs on the timescale of the burst ( $\sim 0.1$  s) due to the vertical expansion of the convective layer caused by thermal diffusion of heat away from the burning layer. Compared to the burst timescale, the convective timescale is many orders of magnitude smaller ( $\sim 1000 \mu\text{s}$  at  $\log \text{EGR}_{max} = 16$ ;  $\sim 150 \mu\text{s}$  at  $\log \text{EGR}_{max} = 19$ ). Thus, a question which arises is whether significant penetration through the formal boundaries of the convective layer occurs on convective timescales. To address this question, transport of test particles through the convective layer boundaries is studied from two perspectives, transport out of and into the convective layer. We say that *under-* and *over-penetration* occurs when test particles originally within the convective layer are carried beyond the lower and upper convective layer boundaries, respectively. Conversely, *bottom-* and *top-penetration* occurs when test particles initially bordering the exterior of the convective layer are carried into the lower and upper boundaries, respectively.

To track the trajectory of tracer particles, the following procedure is performed at five

stages of the burst ( $\log \text{EGR}_{max} = 16, 17, 18, 18.5, \text{ and } 19$ ). At each EGR level, the entire velocity field is obtained at each timestep for several convective turnover times. This time-dependent velocity information is inputted into a separate trajectory analysis algorithm, which evolves the positions of massless tracer particles using the forward-Euler method. Linear, 2D interpolation is employed to determine approximate velocities when positions of particles fall between grid-points on the domain. For each penetration analysis, the positions of two particles for each of the 385 zones in the lateral direction are tracked. Thus, the positions of 770 tracer particles are followed per analysis. Particle trajectories respect the lateral periodicity of the domain, allowing for continuity of motion at the right edge if particles fly off the left edge, and vice versa.

Overall, the results of the tracer particle analyses show that when averaged throughout the burst stages examined, only 10% of the total number of particles penetrate the convective layer boundaries, and when penetration occurs, its extent and duration are limited and temporary. Virtually no under- and over-penetration occurs when  $\log \text{EGR}_{max} < 17$ , but penetration becomes more frequent at higher EGR levels when the formal convective layer boundaries fluctuate rapidly on subconvective timescales. For example, Figure 11 shows a histogram of under- and over-penetration events at  $\log \text{EGR}_{max} = 18.5$ . The number of penetration events is plotted on the vertical axis, while the extent of penetration (in cm) with respect to the time-averaged positions of the lower and upper positions of the convective layer boundaries is plotted on the horizontal axis. Thus, negative values of the extent indicate under-penetration, while positive values, over-penetration. At this particular EGR level, nearly 20% of the particles penetrate the convective layer boundaries, mostly under-penetration events. The majority penetrate less than 10 cm from the lower boundary, but a few are found as far as 25 cm ( $0.15 H_P$ ). Nevertheless, these penetration events are temporary, and the penetrating particles are eventually carried back into the convective layer. This effective trapping of material inside the convective layer may be understood to result from the dominance of lateral over vertical flows at the convective layer boundaries (e.g., see Fig. 6 and discussion in §3.1). Vertical progress of particles inside the convective region halts at the boundaries, since the vertical velocity components diminish by several orders of magnitude there. Stronger lateral flows deflect the particles until they are eventually swept back into the convective region. Bottom- and top-penetration are also very limited. Tracer particles originally above the convective region are found to more easily fall into it, rather than rise up from below. Top-penetration depends very sensitively on the initial positions of the particles. Mixing from beneath the convective layer (dredge-up) is even more limited.

The maximum extent of penetration is found to be  $0.3 H_P$ , which occurs at the bottom boundary at  $\log \text{EGR}_{max} = 19$ , corresponding to a time when flow speeds are relatively large. Modal analysis of select lateral slices of the domain in the manner of Herwig et al.



(2006) reveals that near the convective layer boundaries, a gradual transition from gravity-to convective-modes exists. Thus, convective-modes are always present where penetration occurs. However, they are also present when penetration does not occur. Thus, the presence of convective-modes are necessary but not sufficient for penetration to occur.

### 3.3. Effects of convective energy transport

Here, detailed comparisons of the nuclear flux ( $F_{nuc} = \int_0^{z_{top}} \rho \dot{s}_{3\alpha} dz$ , where  $\dot{s}_{3\alpha}$  is the  $3\alpha$  energy generation rate) between 1D and 2D models are presented. For these comparisons, a 1D model is evolved with the same initial conditions and parameters as the 2D model so that any differences can be directly attributed to the additional mode of energy transfer which convection provides in 2D. The Eddington value of the flux at the surface of a  $1.4 M_\odot$  neutron star of radius  $10^6$  cm is  $F_{Edd} = 2.5 \times 10^{25}$  erg s $^{-1}$  cm $^{-2}$ , assuming electron scattering, and is used as a reference value. In principle, the temporal behavior of  $F_{nuc}$  during an X-ray burst is directly related to the observed light curve, since the burst is powered by the thermonuclear event. However, the present model does not extend up to the actual surface of the neutron star, and the time evolution of  $F_{nuc}$  cannot be rigorously translated into simulated light curves. Nevertheless, many differences distinguish the behavior of  $F_{nuc}$  in the 1D and 2D models and can be attributable to the effects of convective dynamics. Thus, convection in neutron star envelopes arising during a burst may significantly affect what is actually observed, and simulated light curves from numerical calculations of this phenomenon need to properly account for convection.

In Figure 12, the logarithms of  $F_{nuc}/F_{Edd}$  for both the 1D and 2D models are plotted as functions of time. As the figure shows, the 1D and 2D temporal evolution of  $F_{nuc}$  during the burst differs significantly. The total time required to reach burst peak from the beginning of the simulation is delayed 0.36 s for the 2D model (1.57 s vs. 1.21 s). Likewise, the time required for  $F_{nuc}$  to rise from the Eddington value to the peak value is over three times greater in 2D than 1D. Similarly, the time required for  $F_{nuc}$  to diminish from  $F_{nuc,peak}$  to  $e^{-1}F_{nuc,peak}$  in 2D is less than half of what is needed in 1D. These differences can be understood to be the result of convection, which provides an additional mode of energy transfer which enhances thermal transport away from the hottest regions, thus helping to cool and moderate the nuclear runaway.

The factor of 2.5 increase in the magnitude of the peak nuclear flux  $F_{nuc,peak}$  in the 2D model can also be explained by considering the dynamic effects of convection and the accompanying advection. Convection keeps the 2D temperature profile adiabatic. Consequently, the temperature in the upper part of the 2D domain is several times greater as compared

to the same region in the 1D domain, which exhibits a very sharp temperature gradient centered on the burning layer. Convection also directly effects the composition profile, since it thoroughly mixes fuel from upper regions, where  $Y$  is initially greater, to lower regions, where it is hotter. Consequently, by the time of burst peak, more fuel has burnt in 2D. The net result of all these differences is that the EGR in a large part of the the 2D domain exceeds 1D values by many orders of magnitude at burst peak. For example, at burst peak at  $z = 800$  cm in the 1D domain,  $T_{1D} = 2 \times 10^8$  K,  $Y_{1D} = 0.98$ , and  $\log \text{EGR}_{max,1D} = 11$ ; while at the same height in the 2D domain,  $T_{2D} = 5 \times 10^8$  K,  $Y_{2D} = 0.60$ , and  $\log \text{EGR}_{max,2D} = 18$ . Thus, the greater  $F_{nuc,peak}$  in 2D compared to 1D can be understood to be the result of convective and advective effects which exclusively occur in the 2D model. Taken together, these results indicate convection significantly affects energy transport during the burst, resulting in significant differences in the temporal behavior of  $F_{nuc}$  and, presumably, the actual light curve of the burst.

#### 4. Code verification

Extensive verification studies were performed to demonstrate convergence of qualitative and quantitative results of the LMNA model. The model underwent rigorous refinement testing by evolving through complete burst sequences using different spatial resolutions (5, 7.5, 10 cm/zone), temporal resolutions (CFL = 0.5, 0.5/2, 0.5/4), and domain sizes (386×200, 386×205). (The purpose of the small change in domain height in the 386 × 205 model was to test the sensitivity of the solution to the upper boundary’s placement. The domain height cannot be greatly extended without encountering limiting factors associated with lower density regions, such as the severe timestep restrictions required by thermal diffusion.) At four EGR levels leading up to the peak of the burst ( $\log \text{EGR}_{max} = 16, 17, 18, 19$ ), the different models were compared according to the characteristics of key features in the flow fields and how they evolved, the time-evolution of diagnostic thermodynamic and dynamical quantities (such as  $\text{EGR}_{max}$ ,  $T_{max}$ ,  $F_{nuc,max}$ ,  $\mathbf{v}_{max}$ , and  $\mathbf{v}_{ave}$ ), vertical profiles of velocity correlations, and thermodynamic gradients  $\nabla$ ,  $\nabla_{ad}$ , and  $\nabla_L$ . As an example, Figure 13 shows  $\log \text{EGR}_{max}$  as a function of time for three models of 5, 7.5, and 10 cm/zone resolution. The three models attained  $\text{EGR}_{peak}$  values which agreed to within 3%. The times required to attain burst peak ( $t_{peak}$ ) for the 5, 7.5 and 10 cm/zone models are 1.57, 1.63, and 1.73 s respectively, which show a tendency toward convergence with increasing resolution. (The decrease in trend of  $t_{peak}$  can be understood to be the result of a corresponding decrease in numerical dissipation at greater spatial resolutions.) Similarly, other diagnostic quantities which were examined agree to within 5% of the results of the 5 cm/zone model. Moreover, all of the qualitative features of the convective dynamics which developed in this model are reproducible under

the spatial, temporal, and domain refinements which were examined.

## 5. Discussion

The major accomplishments and findings of this project are summarized as follows: (1) The low Mach number approximation has been developed, verified, and implemented to study astrophysical deflagrations where large vertical pressure variations exist and the Mach number  $M$  is small. (2) When applied to subadiabatic initial conditions representing the pre-burst peak stage of a Type I X-ray burst, a vertically expanding convective layer of Bénard-like cells naturally develops, and the vertical extent of the larger cells matches that of the convective layer. The convective layer expands to two pressure scale heights during the burst progression. (3) Even at their maximum values, convective flow speeds are substantially subsonic ( $M_{peak} < 0.15$ ), while the deviation of the pressure from the hydrostatic base state is always at most of order  $M^2$ . (4) As the convective layer expands, fuel is naturally mixed into the convective layer, and mixing within the layer is very efficient. However, at the convective layer boundaries, less efficient mixing results in significant composition gradients, such that  $\nabla$  more closely follows  $\nabla_L$  there. Penetration on convective-timescales is limited and temporary. (5) Both sub- and superadiabaticity are found within the convective layer, but it is slightly superadiabatic on average. (6) Convection significantly affects energy transport.

In the present results, convection develops naturally as a consequence of superadiabatic gradients arising from heat inputted into the system by nuclear burning in a bursting layer. No model for convection is assumed; indeed, we have not been able to establish agreement with the predictions of mixing-length theory. Throughout the burst, the average values of the actual gradient  $\nabla$  are best described as generally between  $\nabla_{ad}$  and  $\nabla_L$ , while the instantaneous values are closer to  $\nabla_L$ . Moreover, some penetration occurs at the convective layer boundaries, where on average,  $\nabla$  clearly deviates from  $\nabla_{ad}$  to conform better to  $\nabla_L$ . Whether the Schwarzschild or Ledoux criteria is satisfied in regions where composition gradients exist in massive stars is still an open question in astrophysics. Semiconvection, a relatively slow mixing caused by composition gradients, is poorly understood, and models which examine the Schwarzschild vs. Ledoux gradients yield conflicting results (Merryfield 1995; Canuto 2000). Moreover, Canuto (2000) demonstrates the Schwarzschild criteria necessarily implies convective overshooting, and the Ledoux criteria also necessarily implies overshooting if convection is non-local. The current model includes all the key elements of convective and semiconvective processes, and it provides an opportunity to further examine this important issue.

Several limitations to our current model should be noted. (1) The contribution of

energy generation  $\dot{s}_{12,\alpha}$  due to subsequent  $\alpha$  captures on  ${}^{12}_6\text{C}$  is neglected in the current computation. Calculations show  $\dot{s}_{12,\alpha}$  becomes important post-burst peak due to the rise in ash concentration  $Z$  as a result of burning, and its inclusion is expected to increase the duration and magnitude of the simulated burst. (2) At more advanced stages of the burst ( $\log \text{EGR}_{\text{max}} \geq 19$ ), the upper convective boundary has reached the upper domain boundary. Comparison with a model which has an extended height shows that dynamical results at these stages may be subject to upper boundary influences. However, these differences were relatively minor and did not affect the qualitative behavior described here. Moreover, because the current model does not include the true surface of the star, observable light curves can not be rigorously calculated. (3) While most of the computational domain remains degenerate throughout the burst sequence, calculations show that degeneracy decreases as the burst progresses, and by the end of the calculation, it begins to be lifted in the upper third of the domain where the densities are smallest. Thus, expansion effects may become important at more advanced stages of the burst, and the current assumption that the base state is time-independent may need to be relaxed to better model the dynamics which arise at these later times. (4) The current model neglects rotation and magnetism. We note that these effects can be incorporated within the Low Mach number formalism, and we expect to address them in future work. Nevertheless, the results presented here describe reasonable qualitative behavior of the flow field as a burst progresses. The substantially subsonic flows arising during the burst, the convective layer filling up with larger cells of roughly the same vertical extent, and the better agreement of  $\nabla$  with  $\nabla_L$  near the convective layer boundaries are likely to describe the behavior when these additional effects are included.

Presently, the LMNA method is a powerful computational tool and has been successfully applied to routinely simulate 2D Type I X-ray burst deflagrations, a problem which has thus far been intractable with other methodologies. Continuing to develop the algorithm will be a vital aspect of future work. Computationally, enhancements may include relaxing the time-independence of the hydrostatic base state, extending the model to 3D, implementing different coordinate systems, incorporating adaptive gridding techniques, and improving the input physics, such as incorporating rotation, more complete nuclear burning networks, and a sub-grid turbulence model. The LMNA model is well-suited to routinely model astrophysical deflagrations which occur during Type I X-ray bursts, the pre-ejection stage of classical novae, the pre-detonation stage of supernovae, and the hydrodynamics and burning in the cores of main sequence stars. The LMNA method represents a useful tool which enables the routine investigation of a wide variety of interesting and important astrophysical questions.

## 6. Acknowledgments

We appreciate constructive comments on the draft of this article by M. Zingale and the anonymous referee. In addition, we also wish to acknowledge the helpful discussions with P. Ricker and other members of the FLASH group at the University of Chicago, E. A. Spiegel, M. M. Mac Low, and A. Heger. This project was supported by NSF grant DMS-0202485. This work was partially supported by the National Center for Supercomputing Applications under grant number DMS-020022N and utilized the Origin2000 Array and the IBM pSeries 690. Other computational resources during model development, testing, and application were also generously provided by the FLASH group at the University of Chicago and the Department of Engineering Sciences and Applied Mathematics at Northwestern University.

## 7. Appendix: The Numerical Procedure for the LMNA

The numerical procedure for the LMNA is outlined in more detail. A more complete description of the computational method can be found in Lin (2006). To enhance readability, the expressions in this Appendix are given in differential form. The Forward-Euler method is used for temporal differencing. As will be pointed out below, standard methods of upwind (advective and first-order convective terms) and central differencing (diffusion,  $gK$ , and second-order convective terms) are used for spatial derivatives. For generality, the equations in this Appendix are expressed in 3D, where the lateral dimensions are  $x$  and  $y$  (or  $i$  and  $j$ ), and the vertical dimension is  $z$  (or  $k$ ). The LMNA model in the present study is limited to 2D, where the  $x$  ( $i$ ) dimension is excluded. All variables have been previously defined in the text.

At time  $t = n$  in zone  $i, j, k$ , the variables are:  $\rho_{(i,j,k)}^{(n)}$ ,  $e_{(i,j,k)}^{(n)}$ ,  $P_{(i,j,k)}^{(n)}$ ,  $T_{(i,j,k)}^{(n)}$ ,  $X_{(i,j,k)}^{(n)}$ , and  $\mathbf{v}_{(i,j,k)}^{(n)}$ . For each timestep, the hydrodynamic equations are solved in the following sequence:

1. Solve for the new composition  $X_{(i,j,k)}^{(n+1)}$  and total reaction rate  $R_{(i,j,k)}^{(n+1)}$ . The continuity equation for each species  $l$  in conservative form is

$$\frac{\partial(\rho X_l)}{\partial t} + \nabla \cdot (\rho \mathbf{v} X_l) = \rho R_l,$$

where  $R_l$  is the Lagrangian time derivative of species  $l$ :  $R_l \equiv \frac{DX_l}{Dt}$ . We expand and use the continuity equation,  $\frac{\partial \rho}{\partial t} + \nabla \cdot (\rho \mathbf{v}) = 0$ , to find the non-conservative form of the composition equation:

$$\frac{\partial X_l}{\partial t} = -\mathbf{v} \cdot \nabla X_l + R_l$$

We operator split this step into two operations: (1) advect by upwinding to a half step,  $t = n + \frac{1}{2}$ , neglecting the burning rate  $R_l$ ; (2) use  $X_{l(i,j,k)}^{(n+\frac{1}{2})}, \rho_{(i,j,k)}^{(n)}, T_{(i,j,k)}^{(n)}$  in the  $3\alpha$  energy generation routine to obtain the updated composition,  $X_{l(i,j,k)}^{(n+1)}$  and  $R_{l(i,j,k)}^{(n+1)}$ , where

$$R_l^{(n+1)} \left( X_l^{(n+\frac{1}{2})}, \rho^{(n)}, T^{(n)} \right) = \frac{X_{l(i,j,k)}^{(n+1)} - X_{l(i,j,k)}^{(n+\frac{1}{2})}}{\Delta t}.$$

2. Solve for the new temperature  $T_{(i,j,k)}^{(n+1)}$ .

It can be shown that

$$\rho \frac{De}{Dt} - \frac{P}{\rho} \frac{D\rho}{Dt} = \rho c_p \frac{DT}{Dt} + -\delta \frac{DP}{Dt} + \sum_l \rho \frac{\partial H}{\partial X_l} R_l,$$

where  $e$  is the internal energy and  $\delta \equiv - \left( \frac{\partial \ln \rho}{\partial \ln T} \right)_P$ . Note that for an ideal gas,  $\delta = +1$ , but for a general gas,  $\delta$  must be explicitly evaluated using partial derivatives from the equation of state. In the LMNA, the base hydrostatic pressure is assumed to be constant in time. Then, equating the right-hand-side to  $Q + \nabla \cdot \kappa \nabla T$  and algebraically manipulating, we obtain the temperature equation:

$$\frac{\partial T}{\partial t} = -\mathbf{v} \cdot \nabla T + \frac{1}{c_p} \left( \dot{s} - \frac{\delta}{\rho} w \rho_h g + \frac{1}{\rho} \nabla \cdot \kappa \nabla T - \sum_l \frac{\partial H}{\partial X_l} R_l \right),$$

where hydrostatic equilibrium  $\nabla P_h = -\rho_h \mathbf{g}$  of the base state is employed.

To update  $T$ , the temperature equation is operator split into separate steps. The advection term is upwinded, while the thermal diffusion term is calculated as two first-order central differences over one zone: i) to determine the negative of the thermal flux  $-F = \kappa \nabla T$  at the edges of a computational zone, and ii) to evaluate  $\nabla \cdot (-F)$  at the zone center. For the thermal diffusion term,  $\kappa(\rho, T, X_l)$ , the radiative thermal conductivity, is  $\kappa = \frac{4}{3} \frac{acT^3}{\kappa_o \rho}$ , where  $\kappa_o(\rho, T, X_l)$  is the radiative opacity, calculated from analytical expressions as referenced in Iben (1975), Christy (1966), and Weaver et al. (1978).

3. Solve for the new density  $\rho_{(i,j,k)}^{(n+1)}$ .

Having updated  $X_{(i,j,k)}^{(n+1)}$  and  $T_{(i,j,k)}^{(n+1)}$ , and assuming  $P_{(i,j,k)}^{(n+1)} = P_{(i,j,k)}^{(n)}$  the equation of state  $EOS(T, P_h, X_l)$  is used to update density  $\rho_{(i,j,k)}^{(n+1)}$  and internal energy  $e_{(i,j,k)}^{(n+1)}$ .

$$\rho_{(i,j,k)}^{(n+1)} \Leftarrow EOS(T, P_h, X_l),$$

$$e_{(i,j,k)}^{(n+1)} \Leftarrow EOS(T, P_h, X_l).$$

4. Solve for  $\phi = P' - gK$  using an elliptic equation, where  $K = \int_{z_{top}}^z \rho'(x, y, z') dz'$ . To derive the elliptic equation, we rewrite the momentum equation in terms of  $\phi$ :

$$\nabla \phi = -\rho \frac{D\mathbf{v}}{Dt} - \left\{ \frac{\partial(gK)}{\partial x} \hat{\mathbf{i}} + \frac{\partial(gK)}{\partial y} \hat{\mathbf{j}} \right\}.$$

Taking the divergence, we obtain an elliptic equation:

$$\nabla^2 \phi = -\nabla \cdot \left( \rho \frac{D\mathbf{v}}{Dt} \right) - \left\{ \frac{\partial^2(gK)}{\partial x^2} + \frac{\partial^2(gK)}{\partial y^2} \right\}.$$

Using the definition of the material derivative  $\frac{D}{Dt} = \frac{\partial}{\partial t} + \mathbf{v} \cdot \nabla$  and the continuity equation,  $(\frac{D\rho}{Dt} = -\rho \nabla \cdot \mathbf{v})$ ,  $\rho \frac{D\mathbf{v}}{Dt}$  can be expressed as:

$$\rho \frac{D\mathbf{v}}{Dt} = \frac{\partial(\rho \mathbf{v})}{\partial t} + \nabla \cdot (\rho \mathbf{v} \mathbf{v})$$

Applying the divergence, and again using the continuity equation,  $\nabla \cdot (\rho \frac{D\mathbf{v}}{Dt})$  can finally be expressed as:

$$\nabla \cdot \left( \rho \frac{D\mathbf{v}}{Dt} \right) = -\frac{\partial^2 \rho}{\partial t^2} + \nabla \cdot \{ \nabla \cdot (\rho \mathbf{v} \mathbf{v}) \}.$$

Thus, the Laplacian of  $\phi$  becomes:

$$\nabla^2 \phi = \frac{\partial^2 \rho}{\partial t^2} - \nabla \cdot \{ \nabla \cdot (\rho \mathbf{v} \mathbf{v}) \} - \left\{ \frac{\partial^2(gK)}{\partial x^2} + \frac{\partial^2(gK)}{\partial y^2} \right\}.$$

This elliptic equation for  $\phi$  is solved using FISHPAK, a package of subprograms for the solution of separable, elliptic partial differential equations developed by Adams, Swarztrauber, and Sweet (1988).

We next consider the detailed evaluation of each of the terms on the right-hand-side of the elliptic equation:

- a.) Using the continuity equation, the time derivative of  $\frac{\partial^2 \rho}{\partial t^2}$  is expressed as

$$\frac{\partial^2 \rho}{\partial t^2} = \frac{1}{\Delta t} \left[ \left( \frac{\partial \rho}{\partial t} \right)^{n+1} + \nabla \cdot (\rho \mathbf{v})^n \right],$$

where at time-level  $n + 1$ ,  $\left( \frac{\partial \rho}{\partial t} \right)^{n+1}$  is calculated analytically from an expression obtained by evaluating the partial derivatives of the internal energy, and at time-level  $n$ ,  $\nabla \cdot (\rho \mathbf{v})^n$  is centrally differenced over two zones. This procedure for calculating  $\frac{\partial^2 \rho}{\partial t^2}$  was found to be required for numerical stability.

b.) By considering its parts and then taking the divergence, a relatively simple and symmetric expression is obtained for  $\nabla \cdot \{\nabla \cdot (\rho \mathbf{v} \mathbf{v})\}$ , which include the convective terms:

$$\begin{aligned} \nabla \cdot \{\nabla \cdot (\rho \mathbf{v} \mathbf{v})\} = & \frac{\partial^2(\rho u^2)}{\partial x^2} + \frac{\partial^2(\rho v^2)}{\partial y^2} + \frac{\partial^2(\rho w^2)}{\partial z^2} \\ & + \frac{\partial}{\partial x} \frac{\partial(\rho uv)}{\partial y} + \frac{\partial}{\partial x} \frac{\partial(\rho uw)}{\partial z} \\ & + \frac{\partial}{\partial y} \frac{\partial(\rho vu)}{\partial x} + \frac{\partial}{\partial y} \frac{\partial(\rho vw)}{\partial z} \\ & + \frac{\partial}{\partial z} \frac{\partial(\rho wu)}{\partial x} + \frac{\partial}{\partial z} \frac{\partial(\rho wv)}{\partial y}. \end{aligned}$$

Each second-order convective term is calculated as two first-order derivatives: i) upwinding is used first to obtain the terms in  $\nabla \cdot (\rho \mathbf{v} \mathbf{v})$ , and ii) these terms are then centrally differenced over one zone to obtain the final expressions in  $\nabla \cdot \{\nabla \cdot (\rho \mathbf{v} \mathbf{v})\}$ .

c.) Derivatives involving  $K$  are centrally differenced.

5. Solve for the new velocity  $\mathbf{v}_{(i,j,k)}^{(n+1)}$ .

From the momentum equation,

$$\frac{\partial(\rho \mathbf{v})}{\partial t} = -\nabla \cdot (\rho \mathbf{v} \mathbf{v}) - \nabla \phi - \left\{ \frac{\partial(gK)}{\partial x} \hat{\mathbf{i}} + \frac{\partial(gK)}{\partial y} \hat{\mathbf{j}} \right\}.$$

The convective terms which had been previously calculated are applied again here. Derivatives involving  $K$  are centrally differenced. Because the domain utilizes a staggered-grid system, the velocity components are determined and stored at zone edges. To determine a zone's central values of the velocity components, the appropriate component's values at the zone edges are spatially averaged

6. Finally, the timestep is complete, and all quantities are updated to  $t = n + 1$ :  
 $\rho_{(i,j,k)}^{(n+1)}, e_{(i,j,k)}^{(n+1)}, P'_{(i,j,k)}{}^{(n+1)}, T_{(i,j,k)}^{(n+1)}, X_{(i,j,k)}^{(n+1)}, \mathbf{v}_{(i,j,k)}^{(n+1)}$ .



## REFERENCES

- Adams, J., Swarztrauber, P., & Sweet, R. 1988, The National Center for Atmospheric Research.
- Almgren, A.S., Bell, J.B., Rendleman, C.A., & Zingale, M. 2006a, ApJ, 637, 922
- Almgren, A.S., Bell, J.B., Rendleman, C.A., & Zingale, M. 2006b, ApJ, in press
- Bannon, P. R. 1996, J. Atm. Sci., 53, 3618
- Bayliss, A., Leaf G.K., & Matkowsky, B.J. 1992, Combust. Sci. Tech., 84, 253
- Bazán, G., Cavallo, R.M., Dearborn, D.S.P., Eggleton, P.P., Dossa, D.D., Keller, S.C., Taylor, A.G., & Turcotte, S. 2003, in ASP Conf. Ser. 293, 3D Stellar Evolution, ed. S. Turcotte et al. (San Francisco: ASP), 1
- Bell, J.B., Day, M.S., Rendleman, C., Woosley, S.E., & Zingale, M.A. 2004a, J. Comput. Phys., 195, 677
- Bell, J.B., Day, M.S., Rendleman, C., Woosley, S.E., & Zingale, M. 2004b, ApJ, 606, 1029
- Bell, J.B., Day, M.S., Rendleman, C., Woosley, S.E., & Zingale, M. 2004c, ApJ, 608, 883
- Bénard, H. 1900, Rev. Gén. Sci. pures et appl., 11, 1261 & 1309
- Bildsten, L. 1995, ApJ, 438, 852
- Canuto, V.M. 2000, ApJ, 534, L113
- Chan, K.L., & Sofia, S. 1987, Science, 235, 465
- Christy, R.F. 1966, ApJ, 144, 108
- Colella, P., & Woodward, P.R. 1984, J. Comput. Phys., 54, 174
- Cumming, A., & Bildsten, L. 2000, ApJ, 544, 453
- Cumming, A. 2004, Nuc. Phys. B, 132, 435
- Dearborn, D.S.P., Lattanzio, J.C., & Eggleton, P.P. 2006, ApJ, 639, 405
- Deupree, R.G. 2000, ApJ, 543, 395
- Fryxell, B., Olson, K., Ricker, P., Timmes, F.X., Zingale, M., Lamb, D. Q., MacNeice, P., Rosner, R., Truran, J.W., & Tufo, H. 2000, ApJS, 131, 273

- Fushiki, I., & Lamb, D.Q. 1987, *ApJ*, 317, 368
- Glatzmaier, G.A. 1984, *J. Comput. Phys.*, 55, 461
- Herwig, F., Freytag, B., Hueckstaedt, R.M., & Timmes, F.X. 2006, *ApJ*, 642, 1057
- Iben, I. 1975, *ApJ*, 196, 525
- Koschmieder, E.L. 1993. *Bénard Cells and Taylor Vortices* (Cambridge: Cambridge University Press)
- Lewin, W. H. G., van Paradijs, J., & Taam, R.E. 1995, in *X-ray Binaries*, ed. W.H.G. Lewin, J. van Paradijs, & E.P.J. van den Deuvel (Cambridge: Cambridge University Press), 175
- Ledoux, P. 1947, *ApJ*, 105, 305
- Lin, D.J. 2006, Ph.D thesis, Northwestern Univ.
- Majda, A., & Sethian, J. 1985, *Combust. Sci. Tech.*, 42, 185
- McGrattan, K.B., Rehm, R.G., & Baum, H.R. 1994, *J. Comput. Phys.*, 110, 285
- McGrattan, K.B., Baum, H.R., Rehm, R.G., Hamins, A., & Forney, G.P. 2000, *Fire Dynamics Simulator - Technical Reference Guide*, NISTIR 6467
- McGrattan, K.B., Baum, H.R., Rehm, R.G., Hamins, A., Forney, G.P., Floyd, J.E., & Hostikka, S. 2004, *Fire Dynamics Simulator, Technical Reference Guide*, NISTIR 1081
- McMurtry, P.A., Jou, W.H., Riley, J.J., & Metcalfe, R.W. 1985, *AIAA J.*, 24, 962
- Merryfield, W.J. 1995, *ApJ*, 444, 318
- Miralles, J.A., Pons, J.A., & Urpin, V.A. 2000, *ApJ*, 543, 1001
- Neleman, G., & Jonker, P. G. 2006, *astro-ph/0605722*
- Ogura, Y., & Phillips, N.A. 1962, *J. Atm. Sci.*, 19, 173
- Schwarzschild, K. 1906, *Göttingen Nachr.*, 13, 41
- Spiegel, E.A., & Veronis, G. 1959, *ApJ*, 131, 442
- Spitkovsky, A., Levin, Y., & Ushomirsky, G. 2002, *ApJ*, 566, 1018

- Strohmayer, T.E., & Bildsten, L. 2006, in *Compact Stellar X-Ray Sources*, ed. W.H.G. Lewin & M. van der Klis (Cambridge: Cambridge Univ. Press), 113
- Taam, R.E. 1985, *Ann. Rev. Nuc. Part. Sci.*, 35, 1
- Timmes, F.X., & Swesty, F.D. 2000, *ApJS*, 126, 501
- Weaver, T.A., Zimmerman, G.B., & Woosley, S.E. 1978, *ApJ*, 225, 1021
- Zingale, M., Timmes, F.X., Fryxell, B., Lamb, D.Q., Olson, K., Calder, A.C., Dursi, L.J., Ricker, P., Rosner, R., MacNeice, P., & Tufo, H.M. 2001, *ApJS*, 133, 1
- Zingale, M., Woosley, S.E., Cumming, A., Calder, A., Dursi, L.J., Fryxell B., Ricker, P. , Rosner, R., & Timmes F.X. 2002, in *AAS Meeting #94.03* (Washington, D.C.:AAS), 955
- Zingale, M., Woosley, S.E., Rendleman, C.A., Day, M.S., & Bell, J.B. 2005, *ApJ*, 632, 1021

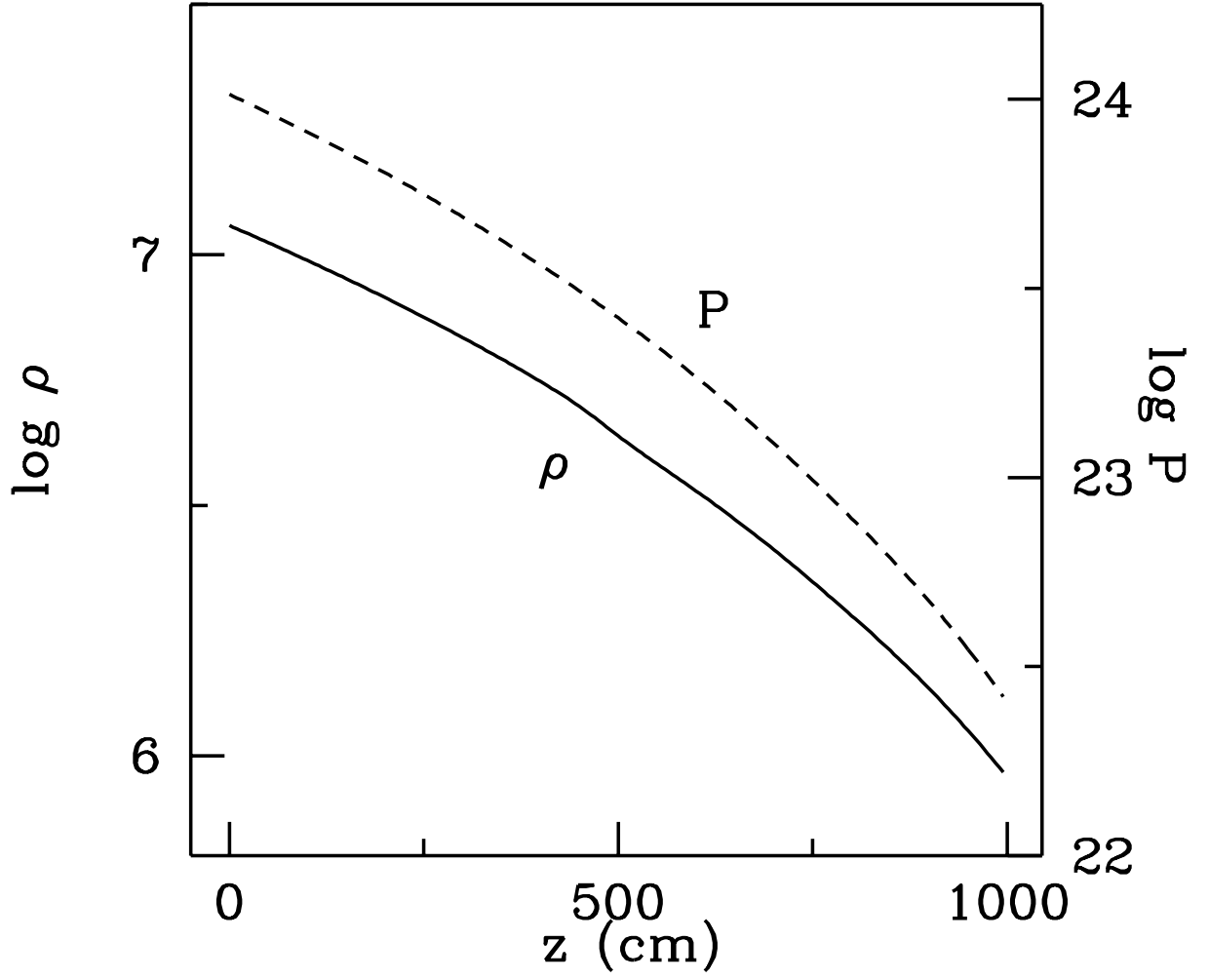


Fig. 1.— Initial  $\rho$  and  $P$ . Initial vertical profile of the 2D domain. The solid line is  $\rho$ , measured on the left axis. The dashed line is  $P$ , measured on the right axis.

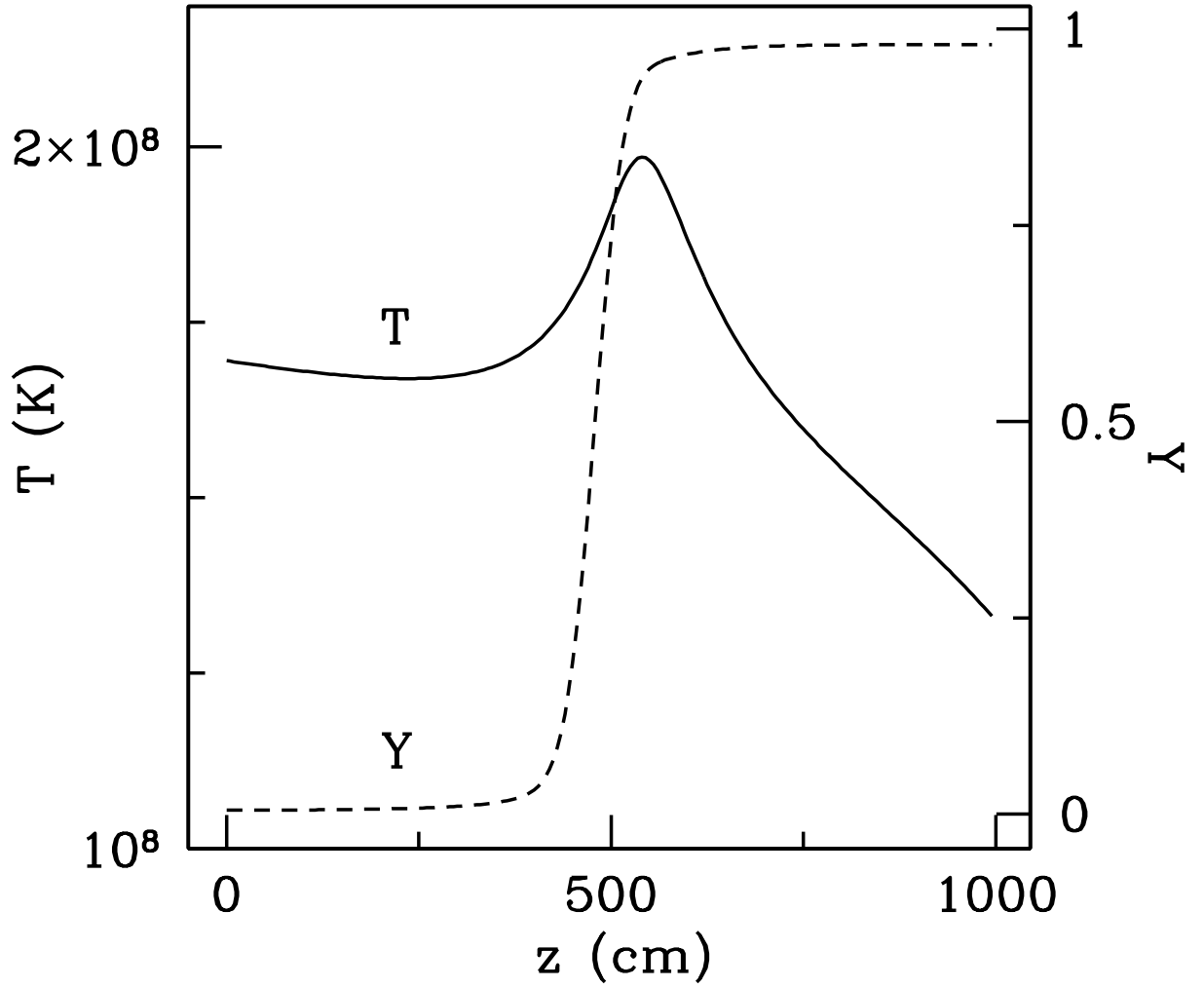


Fig. 2.— Initial  $T$  and  $Y$ . Initial vertical profile of the 2D domain. The solid line is  $T$ , measured on the left axis. The dashed line is  $Y$ , measured on the right axis.

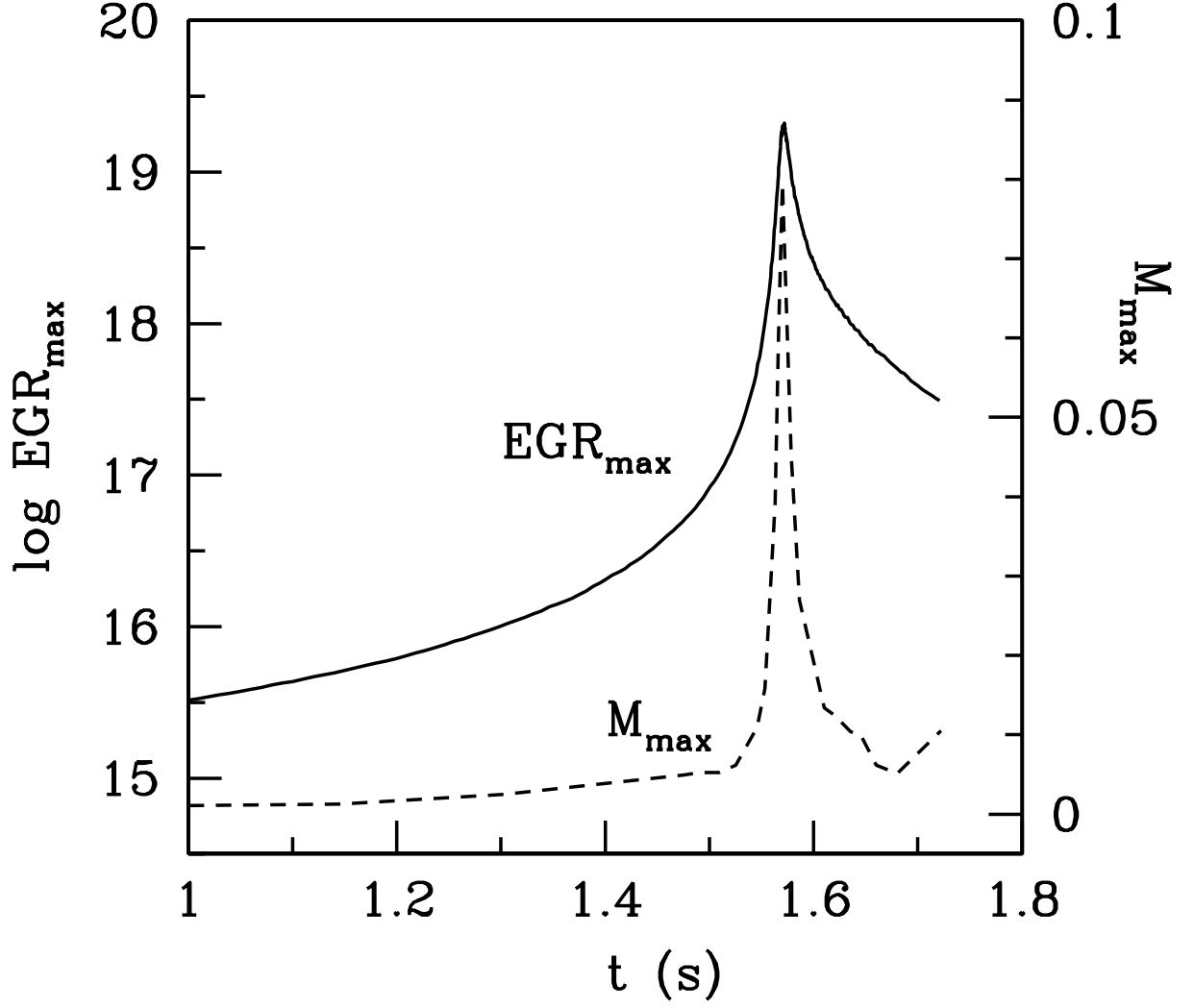


Fig. 3.—  $\log \text{EGR}_{\max}$  and  $M_{\max}$  vs. time (s). Instantaneous maximum values of EGR (solid line, left axis) and Mach number  $M$  (dashed line, right axis) over the entire domain as a function of physical time from the start of the calculation ( $t = 0$  s). Note the peak value of the Mach number is always less than 0.15.

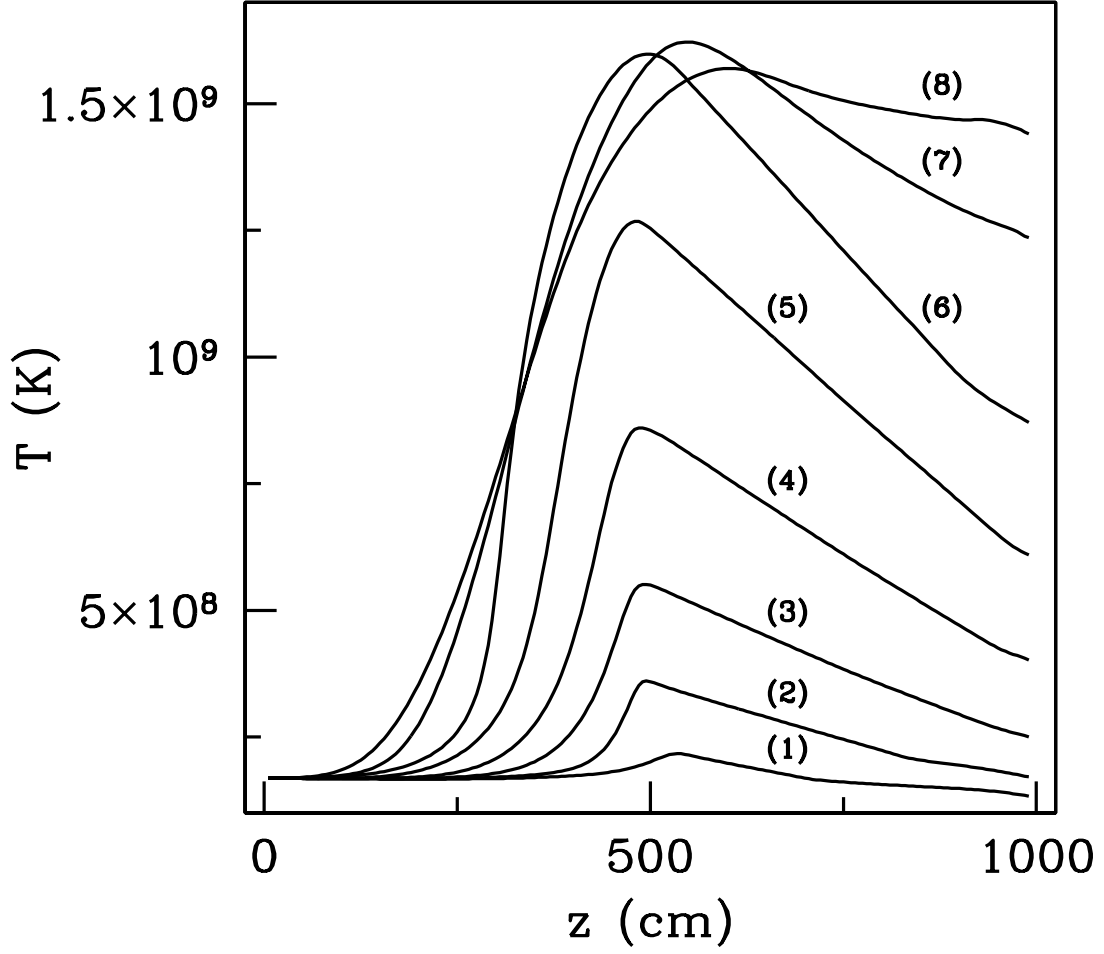


Fig. 4.— Temperature profile at several times. Pre-burst peak, (1) corresponds to  $\log \text{EGR}_{max} = 15.5$ , (2) 18.0, and (3) 19.0. At burst peak, (4) corresponds to  $\log \text{EGR}_{peak} = 19.3$ . Post-burst peak, (5) corresponds to  $\log \text{EGR}_{max} = 18.8$ , (6) 18.0, (7) 17.5, and (8) 17.4.

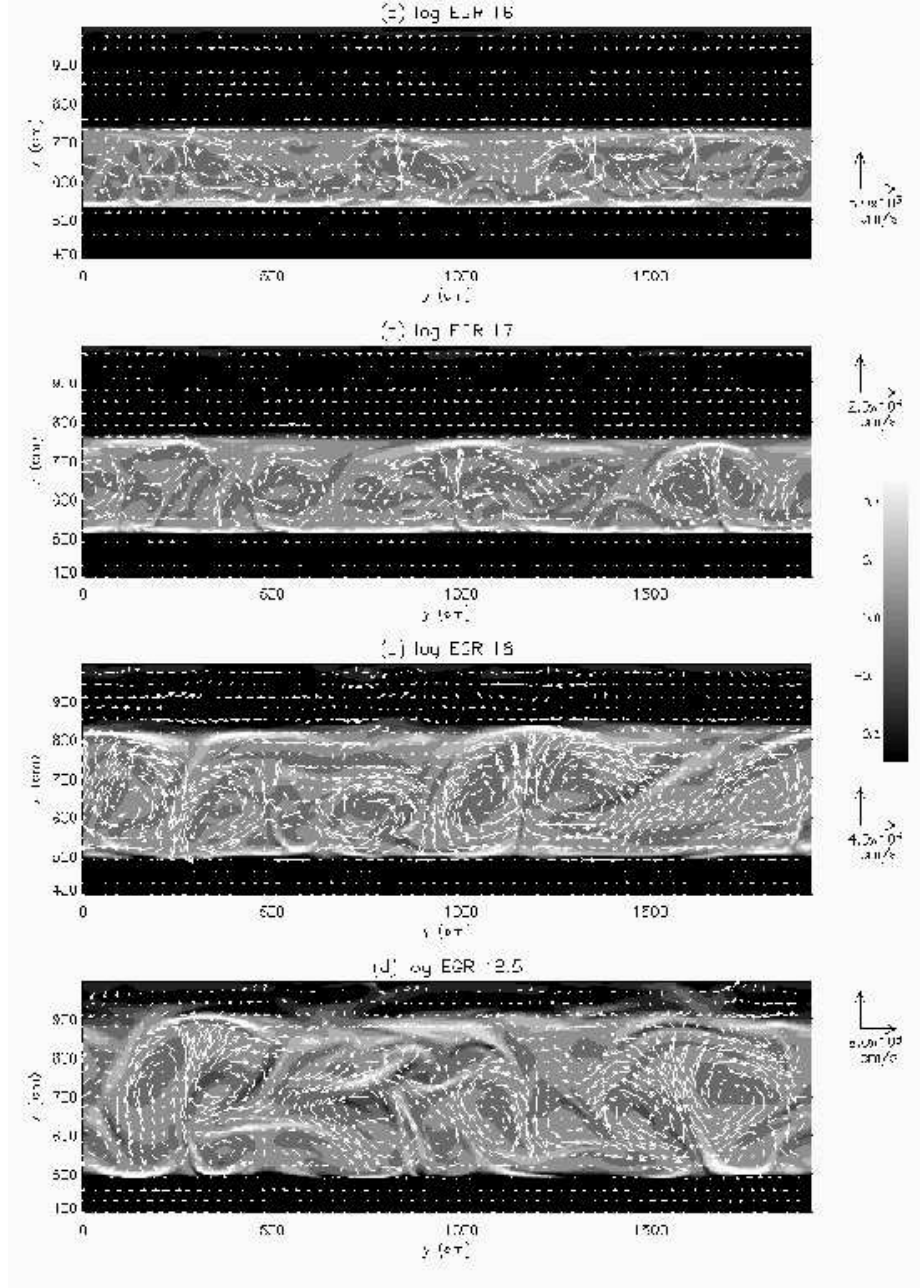


Fig. 5.— Flow fields at four stages of the burst, corresponding to  $\log \text{EGR}_{\max} = 16$  (a), 17 (b), 18 (c), and 18.5 (d). Velocity vectors are superimposed over contours of  $\Delta\nabla$ , the adiabatic excess. Vertical and lateral coordinates given with respect to the lower left corner ( $y = 0, z = 0$ ) of the domain. For clarity, every 6th velocity vector is plotted.



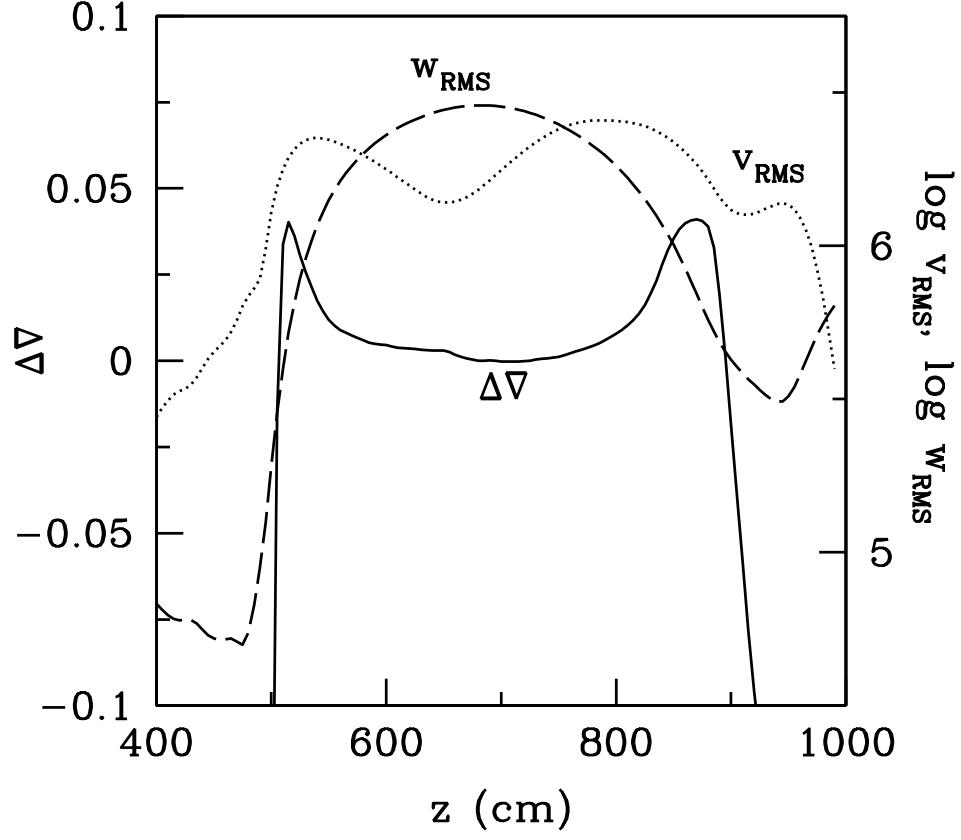


Fig. 6.— Adiabatic excess ( $\Delta\nabla$ ),  $\log v_{RMS}$ , and  $\log w_{RMS}$  vs.  $z$  (cm) at  $\log \text{EGR}_{max} = 18.5$ . The left axis measures  $\Delta\nabla$  (solid line); the right axis measures  $\log v_{RMS}$  (dotted line) and  $\log w_{RMS}$  (dashed line). The magnitudes of vertical speeds range by an order of magnitude within the convective layer ( $\Delta\nabla > 0$ ). At the convective layer boundaries, lateral speeds exceed vertical speeds by an order of magnitude.

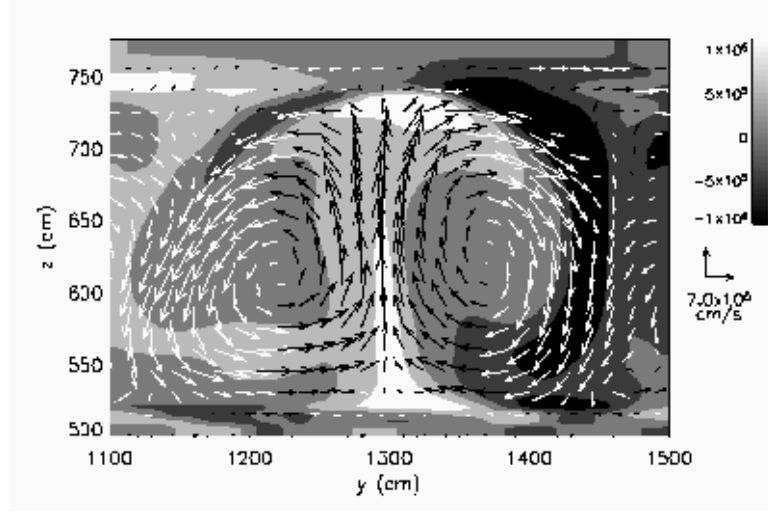


Fig. 7.— Bénard cell at  $\log \text{EGR}_{\max} = 17$ . Velocity vectors are superimposed over contours of  $\Delta T$ , the difference of a zone's temperature compared to the lateral mean. Vertical and lateral coordinates given with respect to the lower left corner ( $y = 0, z = 0$ ) of the domain. Black velocity vectors are used when  $w > 0$ ; white, when  $w < 0$ . Upflows are associated with  $\Delta T > 0$ , while downflows,  $\Delta T < 0$ . Every 3rd velocity vector is plotted.

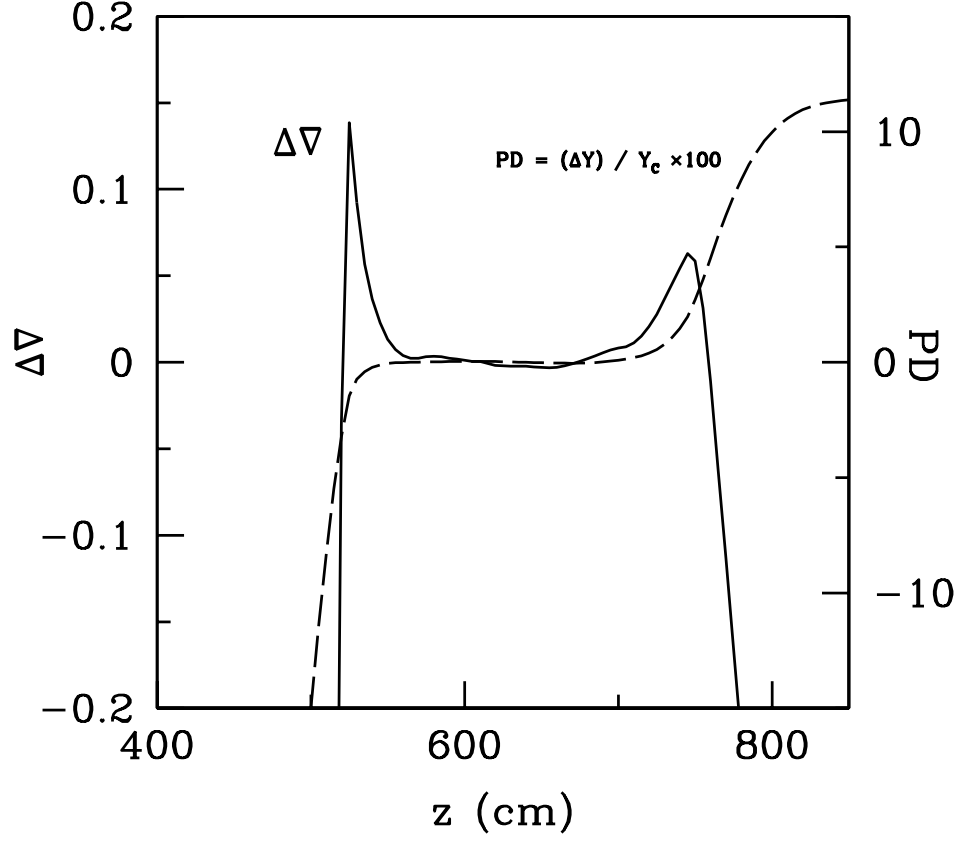


Fig. 8.— Profiles of percentage difference (PD) in  $Y$  and adiabatic excess ( $\Delta \nabla$ ) at  $\log EGR_{max} = 17$ . The left axis and solid line describe  $\Delta \nabla$ , while the right axis and dashed line describe PD. PD is taken with respect to  $Y_C$ , corresponding to  $Y$  at  $z = 625$  cm, the center of the convective layer. While most of the convective layer ( $\Delta \nabla > 0$ ) is well-mixed, significant composition gradients exist at the layer boundaries due to less efficient mixing.

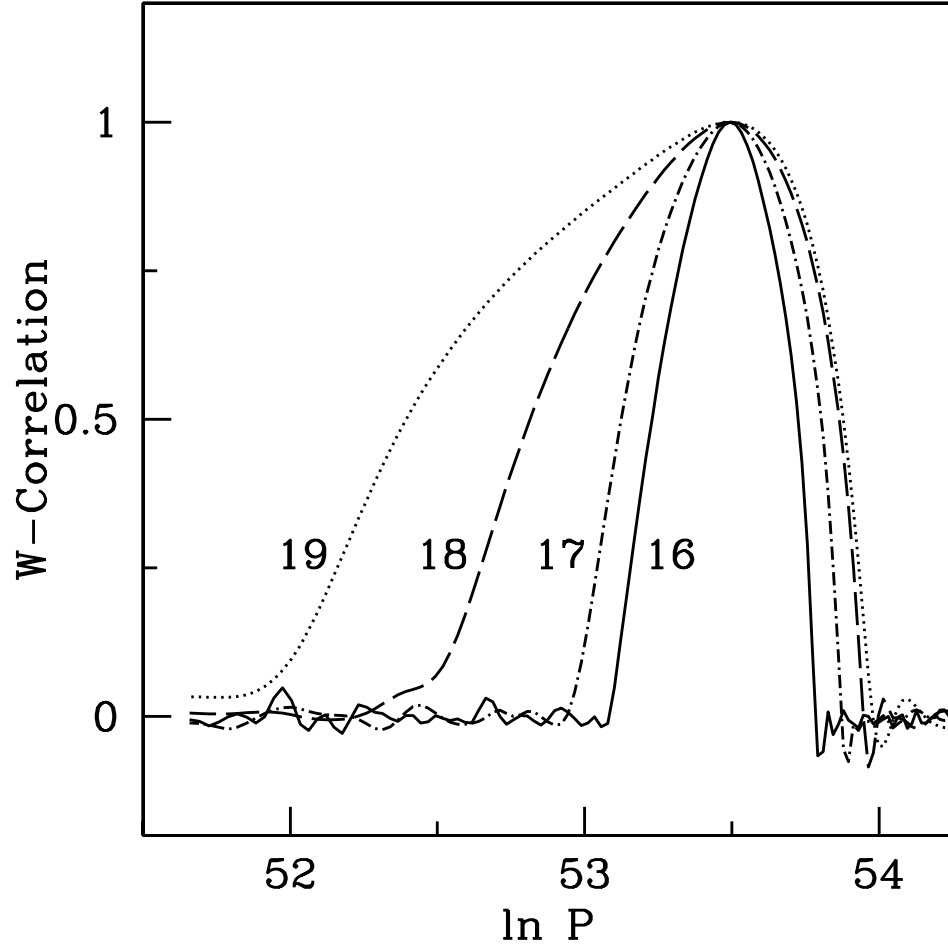


Fig. 9.—  $W$  vs.  $\ln P$ . Taken at four stages during the burst progression:  $\log \text{EGR}_{\max} = 16$  (solid line), 17 (dash-dot-dashed line), 18 (dashed line), and 19 (dotted line). The height of the convective layer increases to two pressure scale heights by  $\log \text{EGR}_{\max} = 19$ . The surface of the star is toward the left of the figure (lower pressures).

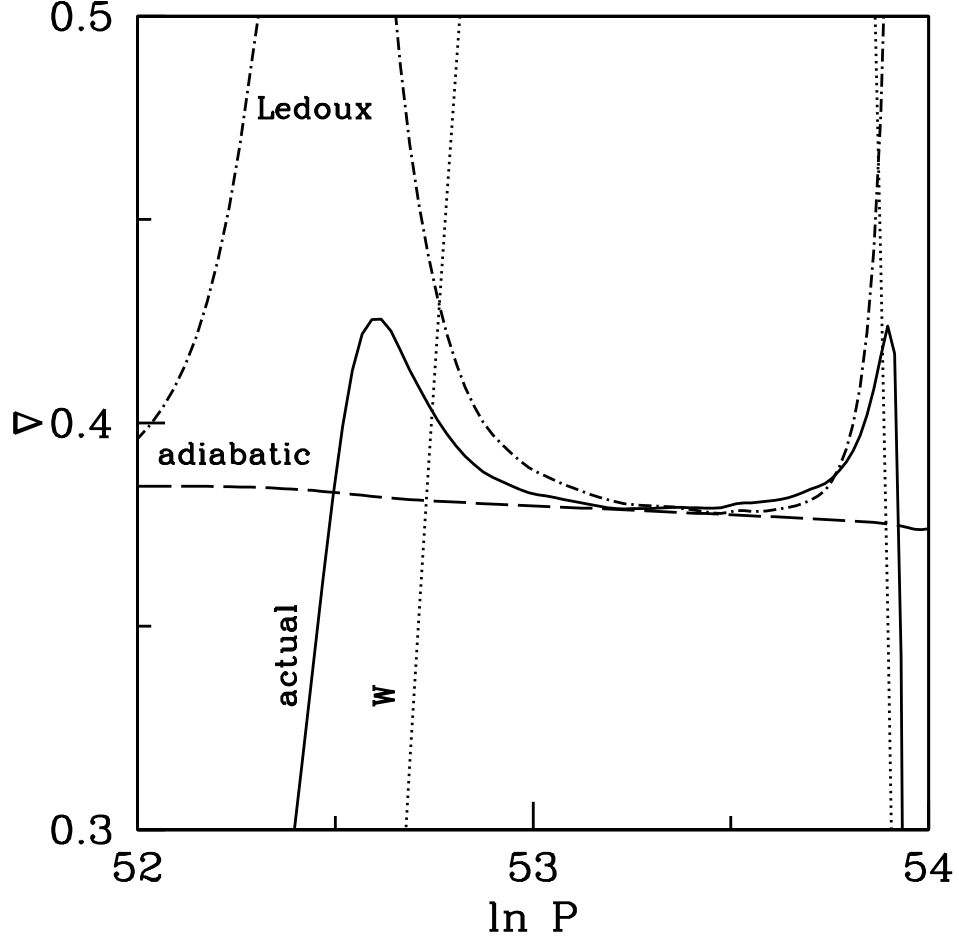


Fig. 10.— Thermodynamic gradients and  $W$  vs.  $\ln P$  at  $\log \text{EGR}_{\text{max}} = 18$ . The solid line is  $\nabla$ , dashed line is  $\nabla_{ad}$ , dash-dot-dashed line is  $\nabla_L$ , and dotted line is  $W$ . The convective region is characterized by a slight adiabatic excess. Near the convective layer boundaries,  $\nabla$  more closely follows  $\nabla_L$ . The surface of the star is toward the left of the figure (lower pressures).

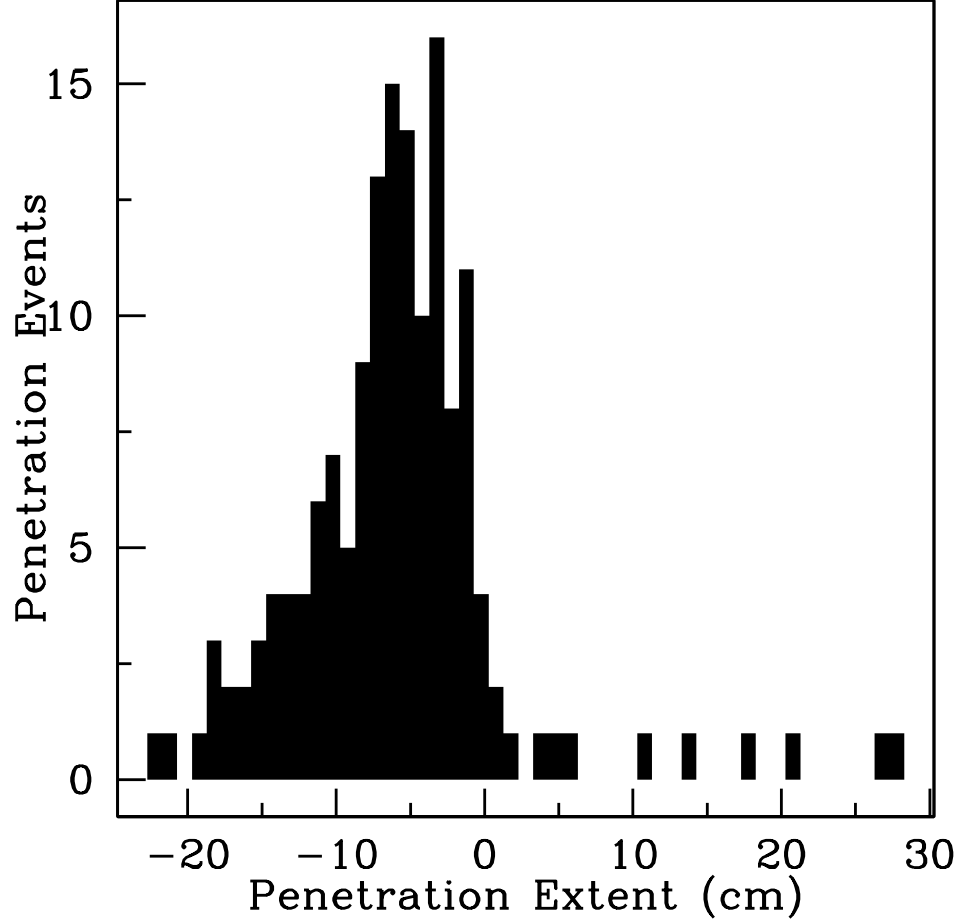


Fig. 11.— Histogram of under- and over-penetration events at  $\log \text{EGR}_{\max} = 18.5$ . Number of events are plotted with respect to the extent, measured in cm with respect to the positions of the lower and upper convective layer boundaries. Negative extents indicate under-penetration, while positive extents, over-penetration.

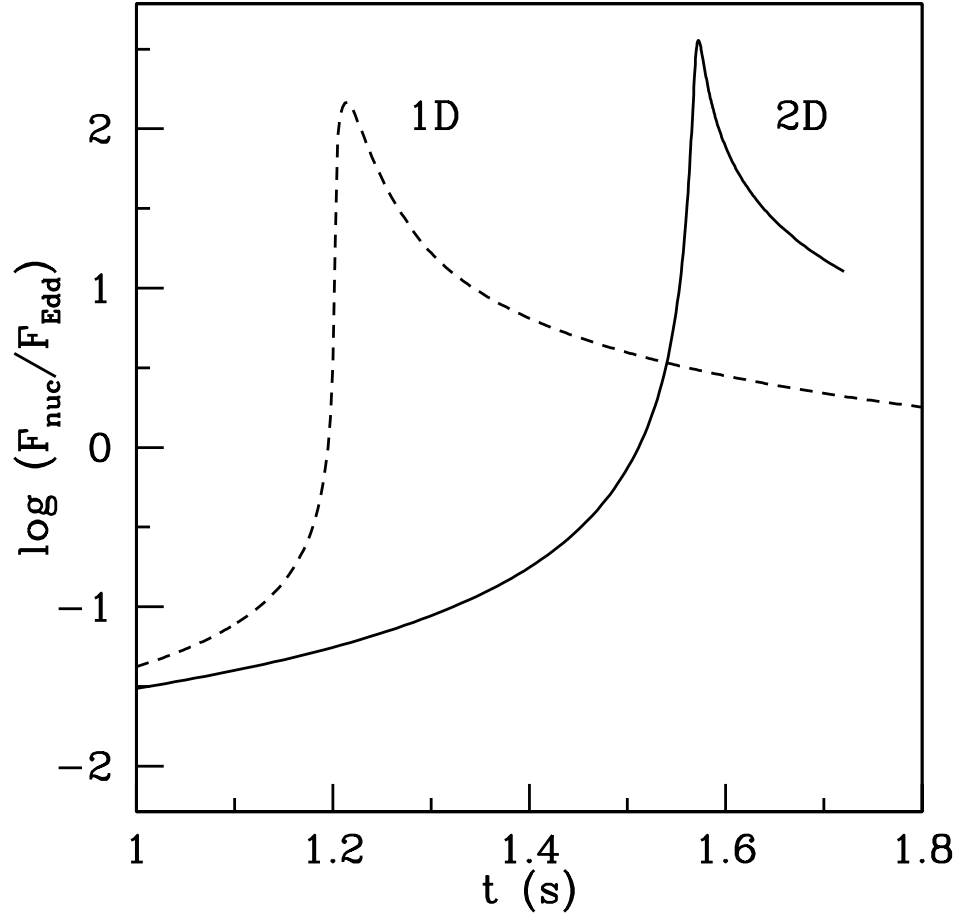


Fig. 12.— 1D, 2D nuclear flux ratio vs. time. The  $\log$  of  $F_{nuc}/F_{Edd}$  for the 1D (dashed line) and 2D (solid line) are plotted as a function of physical time (s) from the start of the calculation ( $t = 0$  s).

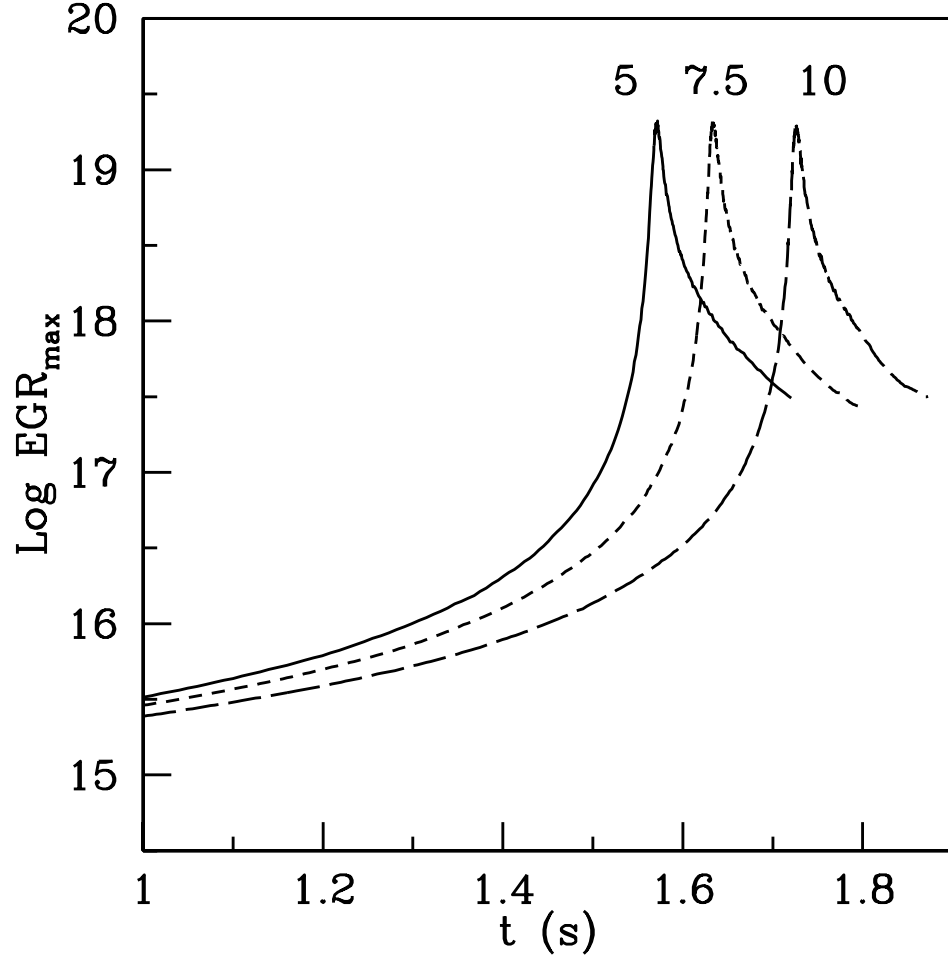


Fig. 13.— Zone-size refinement study. The  $\log$  of  $\text{EGR}_{\max}$  for 5, 7.5, and 10 cm/zone models are plotted as a function of physical time (s) from the start of the calculation ( $t = 0$  s).